Fracture spacings of fiber inclusions in a ductile geological matrix and development of microboudins: 3D numerical modeling

Tiantian Chen[1], Shaocheng Ji[2,*], Chun'an Tang[3], Gillian R. Foulger[4], Bin Gong[5]

1. School of Resources and Civil Engineering, Northeastern University, Shenyang, 110819, China
2. Département des Génies Civil, Géologique et des Mines, École Polytechnique de Montréal, Montréal, Québec, H3C 3A7, Canada
3. State Key Laboratory of Coastal and Offshore Engineering, Dalian University of Technology, Dalian, 116024, China
4. Department of Earth Sciences, Durham University, Science Labs, South Rd., Durham, DH1 3LE, UK
5. Department of Civil and Environmental Engineering, Brunel University London, London UB8 3PH, UK

* Corresponding author (sji@polymtl.ca)

Abstract: Tensile fractures and resultant microboudinage structures of brittle fiber inclusions (e.g., tourmaline, piedmontite and amphibole) in the soft matrix of deforming minerals are of great significance for determining the finite strains and paleostresses of naturally deformed rocks. Using statistical strength theory, damage mechanics, and continuum mechanics, we have reproduced in a series of numerical models the sequential fractures of either homogeneous or heterogeneous fiber inclusions under axial tension in an elastoplastic matrix. The results clarify that: (1) The spacing between fractures in fibers is inversely proportional to the applied strain. As the applied strain increases, the fracture spacing systematically decreases as sequential fractures fill in until fracture saturation is reached. (2) As fiber length increases, the critical tensile strain for fracture saturation rises. For the same fiber diameter, saturation fracture spacing increases slightly with rising fiber length. For the same fiber length, however, saturation fracture spacing decreases significantly with lessening fiber diameter. Hence, fracture spacing at the saturation state depends on the volume fraction of fiber. (3) The rupture mode of fibers strongly depends on the non-uniform distribution of mechanical properties, which provides an effective approach for estimating the inhomogeneity of fibers by analyzing the formation of fractures. Furthermore, due to material heterogeneity, new fractures are unlikely to occur in the

middle of existing adjacent fractures.

Keywords: fracturing, fracture spacing, fiber-matrix composite, boudinage, 3D elastoplastic modeling, tectonic stress, rheology

1. Introduction

Most natural tectonites consist of polymineralic composites, where strong minerals (fibers) are embedded in a weak and ductile matrix (Ji and Xia, 2002; Passchier and Trouw, 2005). For example, tourmaline (Ji and Zhao, 1993; Masuda et al., 2003; Matsumura et al., 2017; Li and Ji, 2020; Li et al., 2020), piedmontite (Masuda and Kuriyama, 1988; Masuda et al., 1989), amphibole (Masuda et al., 2004), and feldspar (Ji and Li, 2021) are typical columnar minerals that experience tensile fracturing within a matrix of plastically deformed minerals, such as quartz. The fiber minerals align parallel to the overall foliation (XY plane normal to Z) and stretching lineation (X) of the deformed rocks, where X, Y, and Z represent the longest, intermediate, and shortest principal axes of the finite strain ellipsoid, respectively (Passchier and Trouw, 2005).

The tensile fractures in the fiber minerals described in the literature (e.g., Masuda et al., 1989, 2003, 2004; Masuda and Kuriyama, 1988; Ji and Zhao, 1993; Matsumura et al., 2017; Li and Ji, 2020; Li et al., 2020) are approximately perpendicular to the elongation direction of the crystals, known as the stretching lineation (Fig. 1). Microstructural observations reported in the aforementioned references have revealed the following characteristics: (a) The fractures in the fiber minerals are generally straight and mutually parallel, lacking pinch and swell structures or plasticity at the edges. This indicates that these fractures are sharp planar cracks resulting from the absence of intracrystalline plasticity during tensile loading (Fig. 1). (b) Minerals with larger aspect ratios (length/width) undergo multiple generations of fractures and exhibit more microboudins compared to those with smaller aspect ratios (Figs. 1a-d). Grains with a critical aspect ratio of approximately 0.8 generally remain unbroken (Li and Ji, 2020; Li et al., 2020). (c) The interboudin gaps, which are filled with soft ductile material (e.g., quartz), are larger for earlier fractures (Figs. 1a-d). However, at low temperatures (<300 °C), the fractured fragments have not yet been separated or filled with matrix minerals such as quartz (Figs. 1e-f). (d) Tensile fractures are typically confined to the fiber minerals (Figs. 1a-d) but occasionally propagate into the surrounding matrix (Figs. 1e-d). (e) Tensile fractures generally do not occur

59 precisely at the center of a columnar grain (Figs. 1a-d).

60 In previous interpretations of mineral microboudins based on the shear-lag theory (e.g., Cox, 1952;
61 Zhao and Ji, 1997; Handge, 2002), mid-point fracturing was commonly assumed (Lloyd et al., 1982;
62 Masuda et al., 1989, 2003; Ji and Zhao, 1993; Matsumura et al., 2017). The shear-lag theory assumes
63 that homogeneous fibers embedded in a matrix do not experience interfacial slip. According to this
64 model, tensile stress in the fiber arises from interfacial shear stress between the fiber and the matrix
65 under axial loading. The continuous extension of the matrix subsequently leads to sequential cracking
66 and fragmentation of the fiber. It is crucial to examine whether the discrepancy between observations
67 (Fig. 1) and theoretical predictions can be largely attributed to the distribution of intrinsic heterogeneity
68 (such as flaws) in the fiber minerals, which influences the initiation and propagation of cracks and
69 varies spatially with the fiber diameter and length.

70 The formation of microboudinage structures through brittle fracturing of fiber minerals within a
71 ductile matrix has garnered significant attention, with numerous studies focused on determining finite
72 strains (Lloyd and Condliffe, 2003), strain rates (Li et al., 2020; Ji and Li, 2021), paleostresses (Masuda
73 et al., 1990; Zhao and Ji, 1997; Matsumura et al., 2017; Li and Ji, 2020; Li et al., 2020; Ji and Li, 2021),
74 and tectonic exhumation history (Ji et al., 1997). However, due to technical challenges in the laboratory
75 (e.g., Etheridge, 1983; Tripathi and Jones, 1998), there have been no tensile fracture experiments
76 conducted on geological fiber-matrix composite materials at high temperature and high pressures.
77 Furthermore, there has been limited numerical research, particularly in three-dimensional (3D)
78 modeling, on the formation processes and key factors influencing the fracture spacing of embedded
79 fibers (Matsumura et al., 2017).

80 In contrast, there has been more numerical research conducted on regularly spaced fractures in
81 layered sedimentary rocks (e.g., Gross et al., 1995; Bai et al., 2000, 2002; Li and Yang, 2007; Tang et
82 al., 2008; Chemenda et al., 2021). These studies have reported that new fractures initiate and propagate
83 between previously formed fractures as the applied load increases. Eventually, all fractures become
84 nearly equally spaced within the homogeneous competent layer, reaching a state of saturation where
85 no new fractures can form even under continuous tension. Instead, the existing fractures continue to
86 open to accommodate the applied strain. When the ratio of fracture spacing to layer length/width
87 exceeds a critical value (approximately 1.0, Bai et al., 2000, 2002), the normal stress in the center of
88 the brittle layer between two opening fractures transitions from tensile to compressive. This stress

transition prevents the formation of further fractures in the center of the layer (Bai et al., 2000, 2002), although new fractures may initiate from the upper and lower boundaries of the bed with the adjacent matrix layers (Li and Yang, 2007; Ji et al., 2021). Nonetheless, the development laws of fractures in heterogeneous fiber minerals at the microscopic scale remain unclear.

While the fundamental principles utilized in numerical models (e.g., Gross et al., 1995; Bai et al., 2000, 2002; Li and Yang, 2007; Tang et al., 2008; Chemenda et al., 2021) are generally accepted, these existing models have limitations in accurately simulating the continuous processes of fracture nucleation, propagation, infilling and saturation that contribute to the formation of microboudinage structures observed in naturally deformed rocks. Fracture infilling refers to the process of creating a new fracture between two neighboring existing fractures in a material, such as a fiber or layer, as long as the fracture density has not reached its saturation state. Previous studies have also overlooked two important mechanisms that could contribute to fracture saturation: the debonding of the fiber-matrix interface and fracturing of the matrix across the layer boundary (Morrison et al., 1988). In materials sciences, debonding refers to the slipping, separation, or detachment of interfaces between different constituent materials within a composite structure (Clyne and Withers, 1993). When debonding occurs, there is a loss of stress transfer efficiency between the materials, which can significantly impact the overall mechanical behavior and strength of the composite. In natural rocks, interlayer slip or interfacial cracks can be categorized as debonding phenomena (Ji et al., 1998; Cooke and Underwood, 2001; Tang et al., 2006; Lyer and Podladchikov, 2009). Despite its importance, systematic and reliable investigations are still required to understand the degree of debonding or coupling between the two mechanically contrasted minerals in deformed rocks, as a consensus has not yet been reached.

It is necessary to point out that most analytical and numerical models have used homogeneous media to simplify geological materials (e.g., 2D models by Gross et al., 1995; Bai et al., 2000, 2002; Tang et al., 2008; Schöpfer et al., 2011; Chemenda et al., 2021; De Joussineau and Petit, 2021; 3D model by Boersma et al., 2018). However, fractures in heterogeneous solids typically originate from scattered microcracks and flaws, which are mechanical weaknesses. This aspect renders the accuracy of homogeneous medium models less reliable, as highlighted by Weibull (1951), Harikrishnan et al. (2018), and Lei et al. (2020). Therefore, the mechanism by which fractures in heterogeneous fibers initiate, grow, and interact with each other until the corresponding fracture morphologies are formed is still not fully understood.

In the present study, we investigated the formation of regularly spaced fractures in fiber inclusions (specifically, tourmaline) embedded in a ductile geological matrix composed of recrystallized quartz aggregates. To achieve this, we established several groups of heterogeneous fiber models based on statistical strength theory, damage mechanics, and continuum mechanics. Subsequently, we numerically captured the progressive fracture process of elastic-brittle fibers within an elastoplastic matrix under axial tension using a three-dimensional (3D) finite element code called RFPA (Rock Failure Process Analysis) (e.g., Tang, 1997; Tang and Tang, 2011; Tang et al., 2020). We robustly examined the dependencies of fracture spacing on average applied strain, fiber length-to-diameter ratio, and material inhomogeneity.

2. Methodology

2.1 Numerical method

The RFPA is a comprehensive three-dimensional rock failure analysis package code based on the finite element method (Tang, 1997; Tang and Hudson, 2010; Tang and Tang, 2011). Since its development in 1997, this code has been extensively utilized in numerous numerical studies on rock mechanics, mining sciences (e.g., Chen et al., 2022; Gong et al., 2022; Wang et al., 2022), materials mechanics (e.g., Tang et al., 2006, 2008), and geology (e.g., Heap et al., 2014, 2015; Wasantha et al., 2014; Griffiths et al., 2017; Pakzad et al., 2018; Tang et al., 2020; Chen et al., 2022), resulting in the publication of over a thousand research papers. Detailed explanations of the method's principles and applications can be found in these earlier papers.

Compared to the numerical methods employed by Gross et al. (1995), Bai et al. (2000, 2002), and Chemenda et al. (2021) for simulating tensile fracture in layered rocks, the RFPA method exhibits several key characteristics. These include: (a) Consideration of heterogeneity in material strength parameters: The RFPA method takes into account variations in the strength properties of the materials involved, acknowledging their heterogeneity. (b) Introduction of elastic modulus reduction for failed elements: When elements fail in the RFPA method, there is a provision to reduce the elastic modulus of those elements accordingly. (c) Progressive recording of the event-rate of failed elements: The RFPA method allows for the continuous recording of the rate at which elements fail during the simulation. (d) Consideration of the degradation of material properties during the deformation process: The RFPA method uses damage mechanics to incorporate the concept of material property degradation as

deformation progresses, enabling a more realistic representation of the fracture process. In the RFPA method, the fracture process is based on the unit element, and therefore, the fracture strength criterion remains consistent for both two-dimensional and three-dimensional scenarios, with the exception of the dimensional increase. However, traditional fracture mechanics methods necessitate mathematical descriptions of specific cracks, making the geometric complexity of three-dimensional cracks more intricate and resulting in more complex equations for fracture description.

In this study, we employed the RFPA method, taking into account fiber heterogeneity, to solve the problem at hand. The relevant material parameters, such as tensile strength, were assumed to follow the statistical distribution described by the Weibull function, based on the 'weakest-link theory' (Weibull, 1951; Harikrishnan et al., 2018; Lei et al., 2020):

$$f(u) = \frac{m}{u_0}\left(\frac{u}{u_0}\right)^{m-1} e^{-\left(\frac{u}{u_0}\right)^m} \quad (1)$$

In this equation, f(u) represents the probability density of the material parameter u, which could be the strength or elastic modulus of an element. The parameter u_0 denotes the average value of u, while m represents the shape coefficient of the distribution function, also known as the material heterogeneity index. According to the definition given by Eq. (1), m should be greater than 1. Figure S1 depicts how the parameters (u) are distributed with increasing material homogeneity index (m) around the average value (u_0). As m increases, the range of distribution becomes narrower, indicating a higher level of material uniformity. Conversely, a lower homogeneity index leads to a wider range of parameter distribution. To further illustrate this, Figure S2 compares the distributions of Young's modulus for a model with a constant u_0 value (56 GPa) but different homogeneity indexes. In Figure S2a, with m=1.2, the distribution of Young's modulus appears complex, and different units exhibit varying u values. However, in Figure S2b, with m=6.0, the distribution of Young's modulus is considerably more uniform, and the differences in u values between units are significantly reduced.

To introduce variation in both strength and elastic modulus, we employed the same probability density function for each model. The Weibull distribution, widely used in fracture mechanics for brittle solids and rocks (Lawn, 1993), is particularly useful for explaining size effects on material strength. Smaller specimens have a lower probability of encountering a large critical flaw (Bažant, 1999; Paterson and Wong, 2005). Therefore, the size effect on material strength is implicitly accounted for in Eq. (1).

In the RFPA method, the stress-strain relationship of a mesoscopic element under uniaxial loading

is shown in Fig. S3. When the stress state of the element satisfies the Mohr-Coulomb failure criteria, damage will occur. Due to gradual degradation as damage progresses, the elastic modulus of the material decreases according to the following equation (Tang et al., 2006):

$$E = (1 - \omega)E_0 \qquad (2)$$

where E and E_0 are the Young's moduli of the damaged and undamaged materials , respectively, and ω is the damage variable.

When the tensile stress borne by one mesoscopic element meets the maximum tensile stress criterion, the damage variable ω is defined by:

$$\omega = \begin{cases} 0 & \varepsilon > \varepsilon_{t0} \\ 1 - \frac{\lambda\varepsilon_{t0}}{\varepsilon} & \varepsilon_{tu} < \varepsilon \leq \varepsilon_{t0} \\ 1 & \varepsilon \leq \varepsilon_{tu} \end{cases} \qquad (3)$$

where λ is the residual strength coefficient which can be defined as $\lambda = \sigma_{tr}/\sigma_{t0}$ where σ_{tr} and σ_{t0} are the residual tensile strength and the tensile strength, respectively; ε_{t0} is the tensile strain corresponding to the elastic limit and initial damage state; and ε_{tu} is the tensile strain corresponding to the ultimate strain and complete damage state (Fig. S3).

When the stress sustained by the mesoscopic element satisfies the Mohr-Coulomb criterion, compressional-shear damage will occur and the damage variable ω can be determined using:

$$\omega = \begin{cases} 0 & \varepsilon < \varepsilon_{c0} \\ 1 - \frac{\lambda\varepsilon_{c0}}{\varepsilon} & \varepsilon \geq \varepsilon_{c0} \end{cases} \qquad (4)$$

where ε_{c0} is the compressive strain corresponding to the elastic limit and the initial damage state (Fig. S3).

In our simulation, the embedded fibers exhibit strain-softening behavior and the initial strength values are distributed according to the Weibull distribution (Weibull, 1951). The numerical computation involves calculating the stress and strain of each element by solving the global equilibrium equation under a quasi-static load. Once the Mohr-Coulomb criterion with a tensile fracture has been met, the element will undergo irreversible failure and its elastic modulus will degrade according to Eq. (2). All elements will follow the above constitutive relation (also see Fig. S3) and strength criteria. Fracture judgment is then repeated as the load increases, enabling the modelling of fracture propagation through continuous element damage.

2.2 Modelling setup

We modeled a 3D cylindrical fiber (i.e., tourmaline) with the length L and cross-section $\pi\times(D/2)^2$ (D is the diameter), fully embedded in a rectangular ductile solid matrix (i.e., quartz). When applying extension parallel to the X-axis (as shown in Fig. 3), stress is transferred from the matrix to the fiber through both the interfacial shear between the fiber and matrix, as well as tension at the end faces of the fiber. The model was validated by comparing calculated stress values and stress state transition between adjacent fractures in the fiber with the microstructural observations of Li and Ji (2020) and Li et al. (2020). The mechanical parameters of tourmaline and quartz used in the simulation are taken from Özkan (1979), McSkimin et al. (1965), Masuda et al. (2003), Kimura et al. (2006) and Matsumura et al. (2017), including the elastic modulus (E), Poisson's ratio (υ), uniaxial tensile/compressive strengths (σ_t/σ_c), residual strength coefficient (λ), heterogeneity index (m) and model size (Table 1).

In the present RFPA simulation, the mechanical properties of the materials are assumed to follow a non-uniform distribution that obeys the Weibull distribution (Weibull, 1951). The degree of material heterogeneity is characterized by the heterogeneity index m, where a larger m indicates a more homogeneous material. To determine the macro-mechanical properties in this study, separate numerical tests of the fiber and matrix were conducted. The resulting stress-strain curves under uniaxial tension (Fig. 2) reveal that the macro-tensile strengths of the elastic-brittle fiber and elastoplastic matrix are approximately 250 MPa and 500 MPa, respectively.

Figures 3a and 3b provide a 3D view of the fiber, model dimensions, and boundary conditions. The cuboid matrix has a total thickness and width of T=4 mm and W=12 mm, respectively. The fiber has a diameter (D) and length (L) of 1 mm and 8 mm, respectively, and is positioned at H=1.5 mm and K=2 mm in Fig. 3b. The model consists of 1,536,000 elements, which ensures precise computational results due to its substantial number of elements. In Fig. 3b, E_f and E_m represent the elastic moduli of the fiber and matrix, respectively, and ν_f and ν_m are the Poisson's ratios of the fiber and matrix, respectively. The left and right boundaries of the model are subjected to displacement-controlled tensile loads with a ratio of 0.0002 mm/step along the X direction, as shown in Fig. 3a.

2.3 Analysis conditions

To assess the accuracy and effectiveness of the fiber model, we investigated the stress

distribution across various fracture spacings. Through numerical simulations, we replicated fracture formation and propagation in fibers with diverse lengths, diameters, and non-homogeneity. The model assumed that the fiber material was in close and strong contact with the outer material, and there was no relative slippage or sliding along the interface. Additionally, the study assumed traction-free conditions at the opening fracture surfaces, which was previously used by Gross et al. (1995), Bai et al. (2000, 2002), and Chemenda et al. (2021). To benchmark the model, the researchers created four parallel fractures with a width of 0.05 mm in the fiber. The study considered fracture spacing (S) and height (D), with D=1 mm and S/D ratios of 0.2, 0.4, 0.6, 0.8, 1.0, 1.2, 1.4, and 2.0.

Figure 3c shows three different sections used to analyze the stress distribution in the model. Section O-O connects the midpoints of the two fractures and is a typical position affected by tensile stress along the axial direction, which was previously studied by Bai et al. (2000, 2002) and Chemenda et al. (2021). Section A-A connects the midpoint of the left end of the fiber and the midpoint of the first fracture on the left, representing the stress state of an unfractured area. Section B-B crosses the area between the two fractures and is close to the upper surface of the substrate, where the interfacial tensile stress between the two fractures is maximum. The model consisted of a fiber with four prefabricated fractures of equal spacing (S) that cut the fiber into five segments along the cross sections. Additionally, the left and right ends of the model were evenly stretched with a stress load of 50 MPa along the X direction. By analyzing the stress distribution of the model at the three representative sections (Fig. 3c), we calculated the stress distributions of the model.

To investigate the relationship between critical fracture spacing and fiber length, we used different fiber lengths (L) of 2 mm, 4 mm, 6 mm, 8 mm, and 10 mm, while keeping the fiber diameter constant at 1 mm. We also explored the relationship between critical fracture spacing and the ratio of fiber length to diameter, using different ratios (L/D) of 2, 4, 6, 8, 10, 15, and 20. To study the effect of fiber heterogeneity, ten different heterogeneity indices (m) of 1.1, 1.3, 1.5, 1.8, 2, 4, 6, 8, 10, and 20 were considered, ranging from non-homogeneous to homogeneous fiber material.

3. Modeling results

3.1 Stress distribution in fibers with prefabricated fractures

3.1.1 Homogeneous fibers

The stress fields in the XZ sections of the models with different fracture spacings and aspect ratios

of homogeneous fibers are presented in Fig. 4 (the maximum principal stress) and Fig. 4S (the minimum principal stress). To analyze the variation of horizontal stress (σ_X) along Section O-O, stress curves were calculated and presented in Figure 5a. The stress state between adjacent fractures is determined by the S/D ratio and the internal stress field. When the S/D ratio is below a critical value, the stress along Section O-O is compressive (positive). Conversely, when the S/D ratio is above the critical value, the stress along Section O-O becomes tensile (negative). The distribution of stress between fractures, as illustrated in Fig. 4 and Fig. 4S, exhibits periodic variations based on the S/D ratio. The critical value of S/D corresponds to the point where the normal stress in the central region between adjacent fractures becomes zero. At this critical point, fracture initiation from the center of the brittle fiber is inhibited.

As the spacing between fractures decreases, the tensile stress between adjacent fractures in the center of the fiber gradually transitions into compressive stress (Figs. 4 and 4S). This transformation hinders the introduction of new fractures from the center of the fiber, where high concentrations of compressive stress impede fracture failure. Similar stress transformations have been documented in previous studies on the fracturing of layered rocks, as reported by Bai et al. (2000), Bai et al. (2002), and Li and Yang (2007). Furthermore, as the fracture spacing gradually decreases, the distribution of compressive stress surrounding the fractures also undergoes changes. For instance, when S/D=1.2, the compressive stress area at the left and right sides of the fractures is significantly reduced (Fig. 4c). This phenomenon becomes more pronounced with the reduction in fracture spacing, mainly due to stress superposition. In other words, the compressive stress is reduced by the tensile stress.

In Figure 5a, the variations of normal stress σ_X along section O-O (Fig. 3c) with increasing S/D are presented. For a fiber with dimensions of D=1 mm, L=8 mm, W=12 mm and T=4 mm, the maximum absolute value of stresses occurs at the midpoint of section O-O. The critical S/D ratio is approximately 0.9, above and below which the normal stress at point C is tensile and compressive, respectively (Fig. 5a). These results suggest that the fiber can be easily fractured due to the infilling of fractures from the center of the fiber before the critical S/D is reached, and that damage cannot occur at the midpoint beyond the critical S/D value. Interestingly, the compressive stress at the midpoint is largest when S/D = 0.6, and an increase or decrease in S/D from this value will result in a reduction in compressive stress (Fig. 5a). Additionally, when S/D = 0.2, the normal stress at any point along Section O-O is zero.

295 The results presented in Fig. 5b suggest that the end segment of the fiber is more susceptible to
296 fracture than the mid-point section. This is because the maximum tensile stress occurs close to the end
297 of the fiber, where the stress concentration is higher. Moreover, the tensile stress along section A-A is
298 higher than along section O-O because the contact area between segment A-A and the matrix is larger.
299 Finally, reducing the S/D ratio or increasing the K/D ratio (where K is the length of the end segment)
300 results in higher tensile stress along section A-A. This is because the interfacial area and thus the
301 segment length are positively correlated with the tensile stress resulting from stress transfer from the
302 matrix to the fiber.

303 Figure 5b illustrates the following important features for section A-A: (1) The normal stress σ_X
304 along this section is everywhere tensile, regardless of S/D value. (2) The maximum tensile stress does
305 not occur at the mid-point of the section but close to the end of fiber (~40% of the A-A length). This
306 suggests that no mid-point fracturing can take place in such an end segment. (3) The maximum tensile
307 stress along section A-A is generally higher than along section O-O. This is because the contact area
308 between segment A-A and the matrix is much larger than between segment O-O and the matrix as long
309 as S/D<2. (4) The tensile stress along section A-A increases with reducing S/D ratio or rising K/D,
310 where the length of the end segment K=(8-3S)/2. The mid-point tensile stress along section A-A also
311 increases with reducing S/D ratio (Figs. 5b and 6b). The reason for this is that the tensile stress, which
312 results from the stress transfer from the incompetent matrix to the competent fiber (Kelley and Tyson,
313 1965; Lloyd et al., 1982; Zhao and Ji, 1997; Masuda et al., 2003), is positively correlated with the
314 interfacial area and thus the segment length.

315 Figure 5c shows that the normal stress σ_X along section B-B is always tensile, regardless of the
316 S/D ratio. The minimum tensile stress occurs at the mid-point of the section and increases gradually
317 with decreasing S/D ratio (Figs. 5c and 6c). These results suggest that when the fractures develop to a
318 certain extent (e.g., S/D≤0.9), interlayer debonding may occur at the interface between the fiber and
319 the matrix, which will prevent further tensile fracturing of the fiber. The tensile stress σ_X at the crack
320 tip (i.e., point B) as a function of S/D ratio shows an asymmetrical dome-shaped variation with a
321 minimum value at S/D=0.72 (Fig. 6d). With the reduction of fracture spacing, new fractures cannot be
322 inserted anymore and the existing fractures can only penetrate vertically toward the substrate due to
323 the presence of crack-tip tensile stresses.
324

3.1.2 Heterogeneous fibers

The presence of heterogeneity in fiber materials introduces small-scale stress fluctuations, which can significantly affect fracture mechanism and failure mode analysis (e.g., Lawn, 1993; Paterson and Wong, 2005). To account for this, we used a more complicated heterogeneous material model for the same geometry shown in Fig. 3c. The stress distribution in this model is shown in Fig. 7, where the dotted lines indicate fluctuations around the mean stress of the homogeneous model (solid lines). These local stress fluctuations may exceed the tensile strength of the material, leading to the formation of new fractures that would not occur in a homogeneous model. Therefore, it is important to consider material heterogeneity when analyzing fracture behavior in fiber materials.

3.2 Initiation, infilling and saturation of fractures in heterogeneous fibers without prefabricated fractures

In this section, we employed the same model as described in section 3.1, but without prefabricated fractures, while considering material heterogeneity. We numerically simulated the initiation and propagation of fractures, as well as the sequential infilling of new fractures. We also analyzed the effects of fiber size and mechanical properties on the fracture evolution process. The process of sequential fracturing continues until saturation is reached, at which point no new fractures can be inserted (Rives et al., 1992; Wu and Pollard, 1995). Our simulation results provide insight into the mechanism underlying sequential fracture infilling and fracture saturation processes in the fibers. In the embedded fiber model, we applied quasi-static, slowly increasing strain until fracture saturation was achieved.

In our simulation, we found that when the matrix is under tension, it can cause stress to build up in the fiber through the fiber/matrix interfacial adhesion. If the accumulated tensile stress exceeds the local tensile strength of the fiber, a fracture will occur at that position. The formation of local fractures releases stress, and new high tensile stress is concentrated between adjacent fractures. If the strength criterion continues to be satisfied, new fractures will be inserted between existing fractures, reducing the fracture spacing. This is known as the stress buildup, stress shadow (e.g., Gross et al., 1995), and stress transfer process (e.g., Ji and Saruwatari, 1998), which collectively lead to the sequential infilling and saturation of fractures in the fiber.

Figure 8 depicts the simulated fracture process under quasi-static, slowly increasing tensile strain with 400 increments from an initial value of 0% to a final value of 0.67%, where each incremental strain is 0.001675%. The process can be divided into four stages based on the sequence of fracture formation. At the first stage (Fig. 8a), initial fractures form randomly and do not interact with each other. During the second stage, six through-going fractures form sequentially (Figs. 8b-g). In the third stage (Figs. 8h-n), seven new fractures initiate between the existing six cracks and propagate before saturation occurs. In the fourth stage (Fig. 8o), fractures keep propagating towards the upper and lower interfaces, penetrating into the matrix due to continuous loading after saturation. All fractures are mechanically constrained by the elastoplastic matrix. A fracture is considered to have occurred when its vertical length reaches 70% of the fiber diameter.

Figure 9 illustrates the number of rupture events that occur during continuous loading. The curve provides a clear visualization of the phenomenon of fracture sequential infilling, as new fractures are added one by one until saturation is reached at a specific tensile strain level of around 0.67%. The graph also reveals that the change in fracture spacing is not continuous, but rather occurs intermittently, despite the continuous increase in tensile strain in the fiber.

3.3 Relationship between fracture spacing and initial length/diameter ratio of heterogeneous fibers

3.3.1 Fracture formation and propagation process

To investigate the relationship between the critical fracture spacing and the fiber length/diameter ratio, we used models with L/D ratios of 2, 4, 6, 8, and 10 mm (Fig. 10). The fiber diameter was held constant at D=1 mm, while the fiber length (L) was varied for each experiment. The model described schematically in Fig. 3 was used, with the material parameters given in Table 1. An axial extension strain was applied with 400 increments, starting from an initial value of 0% and ending at a final value of 0.67%. The modeling results are shown in Figs. 10-11, where it can be seen that mid-point fracturing generally does not occur in fibers with large L/D ratios (≥2, Fig. 10).

Figure 11a depicts the progressive breaking process of fibers with different initial L/D (length/diameter) ratios as the extension strain increases. As the L/D ratio increases, the required critical strain for fracture saturation also increases, making it more difficult for longer fibers to reach fracture saturation if the applied extension strain is insufficient. Furthermore, the strain increment for fracture generation decreases rapidly as the L/D ratio increases. For instance, when L=2, 4, and 6 mm

(with D held constant at 1 mm), fractures occur sequentially with increasing the axial extension strain. In contrast, when L=8 and 10 mm and D=1 mm, fracture generation is remarkably intensive, and more fractures appear rapidly. Consequently, the number of fractures continues to increase until the fiber reaches fracture saturation, and eventually, the fractures penetrate the matrix. Moreover, the number of fractures (Fig. 11b) and the mean fracture spacing-to-diameter ratio (S/D) at saturation display linear relationships with the initial L/D ratio of the fiber (Fig. 11c). The mean S/D ratio ranges from 0.57 to 0.65 when L/D changes from 2 to 10. The reason is straightforward: in a model with a given dimension (i.e., 4×4×12 mm^3), a longer fiber has a higher volume fraction (V_f) than a shorter fiber with the same diameter. As a result, the degree of stress concentration in the fiber becomes significantly higher when the fiber volume fraction is smaller. Therefore, the fracture spacing becomes smaller when the fiber volume fraction is smaller, as illustrated in Fig. 11d.

3.3.2 Change of fragment length during fiber breakage

Figure 12 depicts the process of fiber breaking with an initial length of L=8 mm. The left and right segments resulting from the first fracturing are represented by A1 and B1, respectively. The left and right segments resulting from A1 fracture are A11 and A12, respectively. A1121 and A1122 are the left and right segments of A112 after its breakage, while B12211 and B12212 are the left and right segments of B1221 after its fragmentation. Fracture n (1-13) represents the order of fracture occurrence. According to Fig. 12, the fiber with L=8 mm and D=1 mm underwent 13 fractures, generating 14 microboudins, each of which was less than 0.9 mm. Longer fragments were more susceptible to new fractures, resulting in more fracture events in the longer segments. These modeling results are consistent with previous microstructural observations of naturally deformed rocks (Lloyd et al., 1982; Masuda and Kuriyama, 1988; Masuda et al., 1989, 2003; Ji and Zhao, 1993; Matsumura et al., 2017; Li and Ji, 2020; Li et al., 2020). The reason behind this phenomenon is that longer boudins develop stress concentration more readily, leading to new fractures. Furthermore, fiber segments near the ends broke earlier than the central part (Figs. 10 and 12) due to axial tension, causing the fiber ends with more matrix contacts to peel, resulting in edge damage or near-end fracturing (Ji and Saruwatari, 1998; Ji et al., 1998; Li and Ji, 2020).

Figure 13 illustrates the fracture statistics of fibers with constant diameter (D=1 mm) but different lengths, including L=10, 8, 6, 4, and 2 mm. The ordinate indicates fiber fragment length, while the

414 abscissa represents the order of fracture generation. In Fig. 13d, for instance, the left and right ends of
415 the fiber are represented by 0 mm and 8 mm on the ordinate, respectively. The different colors in the
416 same histogram represent distinct fiber segments. The same color segments indicate that no new
417 fractures occurred in these microboudins. A new fracture typically does not occur at the midpoint of a
418 segment due to material heterogeneity. Fractures occur at the weakest points, which are determined by
419 micro-flaws randomly distributed throughout the entire fiber (Weibull, 1951; Bažant, 1999; Paterson
420 and Wong, 2005). As fiber length increases, the number of fractures and broken fragments also increase
421 (Fig. 13). Additionally, short segments usually occur near the fiber ends.
422
423 3.4 Relationship between fracture spacing and fiber diameter
424 To investigate the relationship between critical fracture spacing and fiber diameter, we considered
425 different ratios of fiber length to diameter (L/D=2, 4, 6, 8, 10, 15, and 20). The fiber length was kept
426 constant at 8 mm, while the diameter varied (Fig. 14). We used the model described in Fig. 3 and the
427 material parameters listed in Table 1. An axial strain load was applied with 400 increments from an
428 initial value of 0% to a final value of 0.67%. Figure 14 illustrates the fracture distribution at saturation
429 in fibers with different L/D ratios. The simulation results show that fracture spacing decreases rapidly
430 at low axial strains, followed by a slow and graduate decrease at high strains. Eventually, the fracture
431 spacing approaches a constant value, which represents the minimum fracture spacing, at saturation.
432 As the diameter of the fiber decreases, the L/D (length-to-diameter) ratio increases, and the fiber
433 volume fraction decreases, the number of fractures generated in the fiber also increases (Fig. 15a). As
434 the L/D ratio continues to increase, both the number of fractures and the growth rate keep rising until
435 the fiber reaches fracture saturation. At this point, the fractures may even penetrate into the matrix
436 material (see Fig. 15b). Figure 15c illustrates that the fracture spacing decreases as the L/D ratio
437 increases, indicating the effect of decreasing fiber volume fraction. The mean fracture spacing varies
438 from 0.96 to 0.48 as the L/D ratio changes from 2 to 20. At saturation, S/D varies linearly with L/D
439 (Fig. 15d). In the model with a given dimension of $6\times6\times12$ mm^3, a thinner fiber (larger L/D ratio)
440 carries comparatively greater stress than a thicker fiber (smaller L/D ratio) with reference to the volume
441 fraction ratio (the fibers have the same lengths). Consequently, the thinner fiber developed a smaller
442 fracture spacing (Fig. 15c).
443

3.5 Effects of material heterogeneity

To investigate the influence of material non-uniformity on fracture mode and spacing, we considered different heterogeneity indices m = 1.1, 1.3, 1.5, 1.8, 2, 4, 6, 8, 10, and 20 (Fig. 16), which represent a transition from a heterogeneous to a homogeneous fiber material. The model presented in Fig. 3 was employed, and axial strain was progressively applied until fracture saturation was reached.

Figure 16 displays the fracture patterns at saturation in 10 fiber models with different heterogeneity indices. As material inhomogeneity changes, fractures exhibit varying modes. In a relatively homogeneous model, the newly formed fractures grow more regularly and visibly, and they tend to cut the fibers perpendicularly. As material heterogeneity increases, more microfractures form and propagate. The primary fractures generally occur through the coalescence of microfractures.

Based on the fracture characteristics observed in the 10 models, they can be classified into two groups for analysis. The first group (m=1.1-2.0, Figs. 16a-e) shows the formation of numerous discontinuous microfractures at weak points during the initial loading. These microfractures then connect and coalesce to form larger fractures, ultimately leading to through-fiber fractures and fiber breakage. As the heterogeneity index m increases, the number of through-fiber fractures also increases. In contrast, the second group (m=4-20, Figs. 16f-j) exhibits a more homogeneous fiber material, with main fractures forming near the middle of fiber segments and being relatively straight and perpendicular to the fiber axis. As the fiber homogeneity increases, scattered microfractures are inhibited, resulting in a more uniform fracture spacing. These fracture characteristics can serve as an indicator of the degree of fiber material uniformity.

4. Discussion

4.1. Two modes of fractures

The mechanical behavior of opening-mode fractures is shown in Fig. 4, where compressive stress concentration is observed in the left and right parts of each fracture opening, while tensile stress is observed at the fracture tip. This phenomenon can be explained as follows. When subjected to lateral stretching, fractures tend to expand toward the tip as they open laterally and shorten vertically. However, high tensile stresses exist in the middle between two adjacent existing fractures and on the interface between the fiber and the matrix. This results in two possible scenarios for fracture development: either the fracture expands into the matrix or a new fracture initiates in between existing

fractures. When the tensile stress at the fracture tip is greater than the tensile strength of the matrix, the fracture will propagate from the tip toward the matrix, a phenomenon that has been observed in naturally deformed rocks (Ji et al., 1997). On the other hand, if the middle tensile stress is greater than the tensile strength of the fiber, new fractures will initiate between the adjacent fractures. Both of these conditions can occur simultaneously in the same system, making them compatible with each other.

4.2. Fracture initiation and saturation

Fracture initiation and propagation in fibers can result in stress redistribution. An important advantage of our simulation is that it does not require any assumptions about the timing and location of new fractures before and after stress redistribution. Moreover, our numerical results demonstrate that fracture initiation can occur at the interface between the fiber and the matrix (Li and Yang, 2007; Chemanda et al., 2021; De Joussineau and Petit, 2021; Ji and Li, 2021), instead of always originating from the center of the fiber (Bai et al., 2000, 2002). As fractures sequentially develop, the distance between adjacent fractures will eventually reach a saturation point, after which no new fractures will form, even under elastoplastic and tensile loading. Typically, as a fracture approaches the interface, the stress at the fracture tip drops below the critical strength, limiting further expansion of the fracture.

The critical aspect ratio (S/D) is an important factor in determining the tensile stress σ_X along different sections (Figs. 5-6), with a critical value of about 0.9 for homogeneous fibers (Fig. 5a). When S/D is larger than the critical value, section O-O is under tensile stress. As fractures infill sequentially or S/D decreases, the tensile stress along the midline decreases. Once the ratio falls below the critical value, the stress state along the midline switches from tensile to compressive. Since the compressive strength of rock materials is much higher than their tensile strength, the infilling of fractures is prevented after the stress changes from tensile to compressive. Under continuous loading, fractures may alternatively develop along the interface between the fiber and the matrix or propagate into the matrix, resulting in either peeling or vertical penetration.

4.3. Corollaries of material heterogeneity

The statistical description of failure phenomena in heterogeneous geological materials has been a topic of interest for decades (Rives et al., 1992; Ji et al., 2021). While material inhomogeneity has been recognized as an important factor in controlling tectonic deformation and failure characteristics, such

as fracture clustering (Weibull, 1951; Becker and Gross, 1996; Horning et al., 1996; Olson, 2004), the mechanisms underlying the formation of regularly-spaced fractures in fiber inclusions are not fully understood (Lloyd et al., 1982; Ji and Zhao, 1993; Zhao and Ji, 1997; Masuda et al., 2003; Matsumura et al., 2017; Li and Ji, 2020; Li et al., 2020). In this study, we successfully captured the influence of material heterogeneity on stress redistribution and buildup, stress shadows, and stress transfer. At the initial stage of fracture morphology development, microfractures primarily started at a small number of diffuse flaws. In relatively homogeneous models (e.g., Gross et al., 1995; Bai et al., 2000, 2002; Li and Yang, 2007; Chemanda et al., 2021; De Joussineau and Petit, 2021), fractures propagate mostly along sections perpendicular to the fiber axis. However, in relatively heterogeneous models, most fractures, initiated from small critical flaws (e.g., Martin et al., 2018), cannot propagate far within the fiber. Occasional connection of microfractures may occur due to local high stress concentrations, eventually leading to the formation of complex fracture structures. Therefore, the heterogeneity-controlled spacing pattern is responsible for fracture clusters documented by Olson (2004) and De Joussineau and Petit (2021).

The theory of fracture saturation in a homogeneous layer, based on the two-dimensional finite element method (Bai et al., 2000, 2002), suggests that new fractures should appear between existing ones, resulting in a continuous halving of fracture spacing, until the stress state at the center of a segment switches from tension to compression. However, our three-dimensional modeling, shown in Figs. 16a-e, clearly indicates that almost no near-perfect halving of fracture spacing occurs. This is due to high material heterogeneity, as new fractures do not necessarily appear in the middle of adjacent fractures. Instead, a segment between two existing fractures may fracture where the local tensile stress exceeds the local tensile strength, rather than at the position of maximum tensile stress. Our modeling results are consistent with microstructural observations of brittle tourmaline microboudins in felsic mylonites (see Fig. 1, Li and Ji, 2020; Li et al., 2020).

The stress distribution between adjacent fractures is primarily influenced by the diameter of the fiber when the length of the fiber remains constant, as shown in Figs. 14-15. On the other hand, when the fiber diameter remains constant, the change in fracture spacing is relatively small as the fiber lengthens, as depicted in Figs. 10-11. The saturation fracture spacing is equally influenced by the L/D ratio of the fiber and increases linearly with increasing fiber length when the fiber diameter is held constant (Figure 11c). However, the saturation fracture spacing decreases linearly with decreasing fiber

diameter when the fiber length remains constant (Figure 15d).

4.4. Limitations of the numerical models within this study

Firstly, the numerical models used in this study assume that the fiber is such a linear and elastic material that fractures suddenly when the applied stress exceeds the elastic limit. Therefore, the modeling results should only be applied to brittle boudins that exhibit planar fracturing, rather than lens-shaped boudins. In the case of ductile boudins that undergo necking or tapering, resulting in pinch and swell geometries, significant ductile strains occur before breaking and separation. Secondly, our current numerical models do not account for the mechanisms of synkinematic cementation, such as mineral precipitation and vein-induced strength recovery, nor do they consider the injection of matrix materials into interboudin gaps. These mechanisms are more complex and will be addressed as a separate topic in our future modeling research. Additionally, it is important to note that the RFPA method requires high computational power for computers. Due to the need for small elements in each computational model to minimize the influence of element size effects, a large number of elements is required, placing high demands on the computational power of the computer. Failure to meet these requirements may affect the accuracy of the computational results.

5. Summary and conclusions

This study aimed to understand regularly-spaced tensile fractures in brittle fiber inclusions (e.g., tourmaline) within a soft matrix (e.g., fine-grained recrystallized quartz aggregate) by establishing several groups of heterogeneous fiber models. The progressive fracture process of strain-softening fibers was successfully simulated using RFPA (Rock Failure Process Analysis) simulation and statistical strength theory, damage mechanics, and continuum mechanics. The study analyzed the relations between fracture spacing and applied strain, fiber length/diameter (L/W) ratio, and material inhomogeneity. The main conclusions are as follows:

(1) Fracture spacing systematically decreases as the applied tensile strain increases, leading to the sequential infilling of new fractures. The tensile stress along the midline between adjacent fractures gradually transforms into compressive stress, creating difficulties in inserting new fractures from the center of the fiber. Once the ratio of fracture spacing to diameter (S/D) of a homogeneous fiber reaches the critical value (approximately 0.90), no new fractures form in the fiber's center, and existing

fractures adapt to additional strain by progressively opening. The reduction in overlapping area significantly diminishes tensile stress, inhibiting the formation of new fractures. As a result, a higher increment of tensile strain is required for further fracture infilling. Furthermore, fractures in the fibers can break the interface and penetrate the matrix, preventing the formation of new fractures in the fiber segments.

(2) The study found that increasing the length of the fiber increases the critical strain required for fracture saturation, making it more difficult for the fibers to reach saturation. As the length-to-diameter ratio of the fiber increases, fractures form more intensively, with more fracture events likely to occur at longer boudins where stress concentration is easier to develop. The study also observed that fiber segments near the ends break earlier than those in the central portion under axial tension, and the number of broken microboudins gradually increases with short microboudins formed near the fiber ends.

(3) The study found that for a fiber with a constant diameter, the mean fracture spacing at saturation decreases linearly with the rising fiber length. On the other hand, for a fiber with a constant length, the mean fracture spacing at saturation decreases linearly with the reduction of the fiber diameter. The study concludes that the saturation fracture spacing increases with the increasing volume fraction of the fiber (V_f), making V_f an important factor influencing the saturation fracture spacing of fibers. A larger V_f reduces the degree of stress concentration in each single fiber.

(4) The study observed that at the initial stage of fracture morphology development, microfractures initiated at mechanical weaknesses or flaws. In a relatively homogeneous model, fractures propagate substantially along sections perpendicular to the fiber axis, but in relatively heterogeneous models, most fractures cannot propagate far within the fiber. Occasionally, the connection of fractures may occur due to local stress concentrations, leading to the formation of a complex fracture structure. The study found that almost no near-perfect halving of fracture spacings occurs, and new fractures generally do not appear exactly in the middle of existing fractures due to material heterogeneity.

Data Availability

The datasets produced and examined are available from the corresponding author on request.

Disclosure statement

The authors declare that they have no known competing financial interests or personal relationships that could have appeared to influence the work reported here.

Acknowledgement

The study acknowledges the funding support provided by the National Natural Science Foundation of China (Grant Nos. 42050201 and 42102314) and the NSERC of Canada (Grant No. 06408). The authors would like to express their gratitude to Dr. Virginia Toy, Dr. Evangelos Moulas, and an anonymous reviewer for their invaluable critical comments and helpful suggestions. Additionally, the authors extend their thanks to Dr. T. Masuda for the insightful discussion and suggestions.

References

Bai, T., Maerten, L., Gross, M.R., Aydin, A., 2002. Orthogonal cross joints: do they imply a regional stress rotation? J. Struct. Geol. 24(1), 77-88.

Bai, T., Pollard, D.D., Gao, H., 2000. Explanation for fracture spacing in layered materials. Nature 403(6771), 753-756.

Bažant, Z.P., 1999. Size effect on structural strength: a review, Archive of applied Mechanics 69, 703-725.

Becker, A., Gross, M.R., 1996. Mechanism for joint saturation in mechanically layered rocks: an example from southern Israel. Tectonophysics 257(2-4), 223-237.

Boersma, Q., Hardebol, N., Barnhoorn, A., Bertotti, G., 2018. Mechanical factors controlling the development of orthogonal and nested fracture network geometries. Rock Mechanics and Rock Engineering 51, 3455-3469.

Chemenda, A.I., Lamarche, J., Matonti, C., Bazalgette, L., Richard, P., 2021. Origin of strong nonlinear dependence of fracture (joint) spacing on bed thickness in layered rocks: mechanical analysis and modeling. J. Geophys. Res.: Solid Earth 126, p.e2020JB020656. https://doi.org/10.1029/2020JB020656

Chen, B.P., Gong, B., Wang, S.Y., Tang, C.A., 2022. Research on zonal disintegration characteristics and failure mechanisms of deep tunnel in jointed rock mass with strength reduction method. Mathematics 10(6): 922

620 Chen, T.T., Foulger, G.R., Tang, C.A., .Mathias, S.A., Gong, B. 2022. Numerical investigation on
621 origin and evolution of polygonal cracks on rock surfaces. Engineering Geology 311, 106913. doi:
622 10.1016/j.enggeo.2022.106913
623 Clyne, T.W., Withers, P.J., 1993. An introduction to metal matrix composites. Cambridge university
624 press.
625 Cooke, M.L., Underwood, C.A., 2001. Fracture termination and step-over at bedding interfaces due to
626 frictional slip and interface opening. J. Struct. Geol. 23, 223-238.
627 Cox, H.L., 1952. The elasticity and strength of paper and other fibrous materials. Br. J. Appl. Phys. 3,
628 72.
629 De Joussineau, G., Petit, J.P., 2021. Mechanical insights into the development of fracture corridors in
630 layered rocks. J. Struct. Geol. 144, 104278.
631 Etheridge, M.A., 1983. Differential stress magnitudes during regional deformation and metamorphism:
632 upper bound imposed by tensile fracturing. Geology 11, 231-234.
633 Gong, B., Wang, Y.Y., Zhao, T., Tang, C.A., Yang, X.Y., Chen, T.T., 2022. AE energy evolution during
634 CJB fracture affected by rock heterogeneity and column irregularity under lateral pressure.
635 Geomatics, Natural Hazards and Risk 13: 877-907.
636 Griffiths, L., Heap, M.J., Xu, T., Chen, C.F. and Baud, P., 2017. The influence of pore geometry and
637 orientation on the strength and stiffness of porous rock. J. Struct. Geol. 96, 149-160.
638 Gross, M.R., Fischer, M.P., Engelder, T., Greenfield, R.J., 1995. Factors controlling joint spacing in
639 interbedded sedimentary rocks: integrating numerical models with field observations from the
640 Monterey Formation, USA. Geol. Soc. Spec. Publ. 92(1), 215-233.
641 Handge, U.A., 2002. Analysis of a shear-lag model with nonlinear elastic stress transfer for sequential
642 cracking of polymer coatings. J. Mater. Sci. 37, 4775-4782.
643 Harikrishnan, R., Mohite, P.M., Upadhyay, C.S., 2018. Generalized Weibull model-based statistical
644 tensile strength of carbon fibres. Archive of Applied Mechanics 88, 1617-1636.
645 Heap, M.J., Xu, T., Chen, C.F., 2014. The influence of porosity and vesicle size on the brittle strength
646 of volcanic rocks and magma. Bulletin of Volcanology 76, 1-15.
647 Heap, M.J., Xu, T., Kushnir, A.R., Kennedy, B.M., Chen, C.F., 2015. Fracture of magma containing
648 overpressurised pores. Journal of Volcanology and Geothermal Research 301, 180-190.
649 Hornig, T., Sokolov, I.M., Blumen, A., 1996. Patterns and scaling in surface fragmentation processes:

650 Physical Review E 54, 4293–4298.
651 Iyer, K., Podladchikov, Y.Y., 2009. Transformation-induced jointing as a gauge for interfacial slip and
652 rock strength. Earth Planet. Sci. Lett. 280, 159-166.
653 Ji, S., Li, L., 2021. Feldspar microboudinage paleopiezometer and its applications to estimating
654 differential stress magnitudes in the continental middle crust (examples from west Yunnan,
655 China). Tectonophysics 805, p.228778.
656 Ji, S., Saruwatari, K., 1998. A revised model for the relationship between joint spacing and layer
657 thickness. J. Struct. Geol. 20, 1495-1508.
658 Ji, S., Xia, B., 2002. Rheology of polyphase earth materials. Polytechnic International Press, Montreal,
659 Canada.
660 Ji, S., Zhao, P., 1993. Location of tensile fracture within rigid-brittle inclusions in a ductile flowing
661 matrix. Tectonophysics 220, 23–31.
662 Ji, S., Zhao, P., Saruwatari, K., 1997. Fracturing of garnet crystals in anisotropic metamorphic rocks
663 during uplift. J. Struct. Geol. 19, 603-620.
664 Ji, S., Zhu, Z., Wang, Z., 1998. Relationship between joint spacing and bed thickness in sedimentary
665 rocks: effects of interbed slip. Geol. Mag. 135, 637-655.
666 Kelly, A., Tyson, W.R., 1965. Tensile properties of fibre-reinforced metals: copper/tungsten and
667 copper/molybdenum. J. Mech. Phys. Solids 13, 329-350.
668 Kimura, N., Awaji, H., Okamoto, M., Matsumura, Y., Masuda, T., 2006. Fracture strength of
669 tourmaline and epidote by three-point bending test: application to microboudin method for
670 estimating absolute magnitude of palaeodifferential stress. J. Struct. Geol. 28, 1093-1102.
671 Lawn, B., 1993. Fracture of Brittle Solids – Second Edition. Cambridge University Press.
672 Lei, W.S., Zhang, P., Yu, Z., Qian, G., 2020. Statistics of ceramic strength: Use ordinary Weibull
673 distribution function or Weibull statistical fracture theory? Ceramics International 46, 20751-20768.
674 Li, L., Ji, S., 2020. On microboudin paleopiezometers and their applications to constrain stress
675 variations in tectonites. J. Struct. Geol. 130, p.103928. https://doi.org/10.1016/j.jsg.2019.103928
676 Li, L., Ji, S., Lin, W., 2020. Tourmaline microboudinage: An indicator of its host rheology. J. Struct.
677 Geol. 138, p.104096.
678 Li, Y., Yang, C., 2007. On fracture saturation in layered rocks. Int. J. Rock Mech. Min. Sci. 44(6), 936-
679 941.

Lloyd, G.E., Condliffe, E., 2003. 'Strain Reversal': a Windows™ program to determine extensional strain from rigid–brittle layers or inclusions. J. Struct. Geol. 25, 1141–1145.

Lloyd, G.E., Ferguson, C.C., Reading, K., 1982. A stress-transfer model for the development of extension fracture boudinage. J. Struct. Geol. 4, 355–372.

Martin, E., Leguillon, D., Sevecek, O., Bermejo, R., 2018. Understanding the tensile strength of ceramics in the presence of small critical flaws. Engineering Fracture Mechanics 201, 167-175.

Masuda, T., Kimura, N., Fu, B., Li, X., 2004. Validity of the microboudin method for palaeostress analysis: application to extraordinarily long sodic amphibole grains in a metachert from Aksu, China. J. Struct. Geol. 26, 203–206.

Masuda, T., Kimura, N., Hara, Y., 2003. Progress in microboudin method for palaeostress analysis of metamorphic tectonites: application of mathematically refined expression. Tectonophysics 364, 1–8.

Masuda, T., Kuriyama, M., 1988. Successive "mid-point" fracturing during microboudinage: an estimate of the stress-strain relation during a natural deformation. Tectonophysics 147, 171–177.

Masuda, T., Shibutani, T., Igarashi, T., Kuriyama, M., 1989. Microboudin structure of piedmontite in quartz schists: a proposal for a new indicator of relative palaeodifferential stress. Tectonophysics 163, 169–180.

Masuda, T., Shibutani, T., Kuriyama, M., Igarashi, T., 1990. Development of microboudinage: an estimate of changing differential stress with increasing strain. Tectonophysics 178, 379–387.

Matsumura, T., Kuwatani, T., Masuda, T., 2017. The relationship between the proportion of microboudinaged columnar grains and far-field differential stress: a numerical model for analyzing paleodifferential stress. J. Mineral. Petrol. Sci. 112, 25–30.

McSkimin, H.J., Andreatch Jr, P., Thurston, R.N.L., 1965. Elastic moduli of quartz versus hydrostatic pressure at 25 ° and −195.8 °C. J. Appl. Phys. 36, 1624-1632.

Morrison, J.K., Shah, S.P., Jenq, Y.S., 1988. Analysis of fiber debonding and pullout in composites. J. Eng. Mech. 114(2), 277-294.

Olson, J.E., 2004. Predicting fracture swarms—The influence of subcritical crack growth and the crack-tip process zone on joint spacing in rock. Geological Society, London, Special Publications 231(1), 73-88.

Özkan, H., 1979. Elastic constants of tourmaline. J. Appl. Phys. 50, 6006-6008.

710 Pakzad, R., Wang, S.Y., Sloan, S., 2018. Numerical study of the failure response and fracture
711 propagation for rock specimens with preexisting flaws under compression. International Journal of
712 Geomechanics 18(7), p.04018070.
713 Parvizi, A., Bailey, J.E., 1978. On multiple transverse fracturing in glass fibre epoxy cross-ply laminate:
714 Journal of Materials Science 13, 2131–2136.
715 Passchier, C.W., Trouw, R.A.J., 2005. Microtectonics. Springer, Berlin.
716 Paterson, M.S., Wong, T.F., 2005. Experimental rock deformation-the brittle field. Springer Science
717 & Business Media, Berlin, Germany.
718 Rives, T., Razack, M., Petit, J.P., Rawnsley, K.D., 1992. Joint spacing: analogue and numerical
719 simulations. J. Struct. Geol. 14(8-9), 925-937.
720 Schöpfer, M.P., Arslan, A., Walsh, J.J., Childs, C., 2011. Reconciliation of contrasting theories for
721 fracture spacing in layered rocks. J. Struct. Geol. 33, 551-565.
722 Tang C.A., Hudson, J.A., 2010. Rock failure mechanisms: illustrated and explained. CRC Press,
723 London.
724 Tang C.A., Liang, Z.Z., Zhang, Y.B., 2008. Fracture spacing in layered materials: A new explanation
725 based on two-dimensional failure process modeling. American Journal of Science 308, 49-72.
726 Tang C.A., Tang, S., 2011. Applications of rock failure process analysis (RFPA) method. Journal of
727 rock mechanics and geotechnical engineering 3, 352-372.
728 Tang, C., 1997. Numerical simulation of progressive rock failure and associated
729 seismicity. International Journal of Rock Mechanics and Mining Sciences 34, 249-261.
730 Tang, C.A., Webb, A.A.G., Moore, W.B., Wang, Y.Y., Ma, T.H., Chen, T.T., 2020. Breaking Earth's
731 shell into a global plate network. Nature communications 11(1), 1-6.
732 Tang, C.A., Zhang, Y.B., Liang, Z.Z., Xu, T., Tham, L.G., Lindqvist, P.A., Kou, S.Q., Liu, H.Y., 2006.
733 Fracture spacing in layered materials and pattern transition from parallel to polygonal
734 fractures. Physical Review E, 73, 056120.
735 Tripathi, D., Jones, F.R., 1998. Single fibre fragmentation test for assessing adhesion in fibre reinforced
736 composites. J. Mater. Sci. 33, 1-16.
737 Wang, Y., Gong, B., Tang, C.A. and Zhao, T., 2022. Numerical study on size effect and anisotropy of
738 columnar jointed basalts under uniaxial compression. Bulletin of Engineering Geology and the
739 Environment 81, 1-33.

Wasantha, P.L.P., Ranjith, P.G., Xu, T., Zhao, J. and Yan, Y.L., 2014. A new parameter to describe the persistency of non-persistent joints. Engineering geology, 181, 71-77.

Weibull, W., 1951. A statistical distribution function of wide applicability. J. Appl. Mech. 18(3), 293-297.

Wu, H., Pollard, D.D., 1995. An experimental study of the relationship between joint spacing and layer thickness. J. Struct. Geol. 17(6), 887-905.

Zhao, P.L., Ji, S., 1997. Refinements of shear-lag model and its applications. Tectonophysics 279, 37–53.

Figure captions

Fig. 1. Extension fractures in tourmaline (a-d) within granitic mylonites from the Chongshan shear zone, Yunnan, China, and garnet (e-f) in quartzitic mylonites from the Morin shear zone, Quebec, Canada. Abbreviations: Gt: Garnet; Qtz: Quartz; Tur: Tourmaline. Some fractures extend into the surrounding quartz matrix in (e-f). See the text for interpretation.

Fig. 2. Material macro-strength test: (a) fiber and (b) matrix. Compressive stress is positive and tensile stress is negative. It is necessary to point out that the values are lower than those listed in Table 1 due to the presence of flaws.

Fig. 3. Schematic diagrams of the model. In (a), a 3D view showcases a cylindrical fiber (depicted in white) embedded within the matrix (represented in gray). The model configuration is illustrated in (b), while (c) showcases the model with four prefabricated fractures. Detailed investigations of stress distributions along sections AA, BB, and OO are carried out.

Fig. 4. Cloud diagram showing the maximum principal stress for models with different ratios of fracture spacing to fiber diameter (S/D). The sections are cut parallel to the X- and Z-axes. The dimensions of the model are 4×4×12 mm^3 and the model unit is 120×120×360=5,184,000. The color-scale in the diagram represents different stress magnitudes.

Fig. 5. Distribution curves of normal stress along sections O-O (a), A-A (b) and B-B (c). Compressive stress is positive and tensile stress is negative. See the text for explanation.

Fig. 6. Distributions of normal stresses as a function of S/D ratio at midpoints of sections O-O (a), A-A (b) and B-B (c) and at crack tips (point B). Compressive stress is positive while tensile stress is negative.

Fig. 7. Distribution of normal stress along section O-O for fibers with different S/D ratios. Dotted lines represent inhomogeneous materials (m=2) whereas solid lines represent homogeneous materials (m=100). Compressive stress is positive and tensile stress is negative.

Fig. 8. Cloud diagrams of maximum principal stress for sequential fracture infilling and fracture saturation of a fiber. The model size is 4×4×12 mm^3, model unit is 80×80×240=153,600, fiber length (L) is 8 mm, fiber diameter (D) is 1 mm and heterogeneity indices m=4 and 6 for fiber and matrix, respectively. Material parameters are listed in Table 1. Red and orange-red represent tensile stresses while yellow, green and blue represent compressive stresses. Numbers indicated in each sub-figure represent the occurrence sequence of fractures.

Fig. 9. Breaking process curves of the fiber with increasing tensile strain. Number of fractures are indicated.

Fig. 10. Fracture distribution in fibers (m=4) with different L/D ratios at saturation. The dimension of the model is 4×4×12 mm^3 and model unit is 80×80×240. Red and orange-red represent tensile stresses while yellow, green and blue represent compressive stresses. Number indicated in each sub-figure represents the occurrence sequence of fractures.

Fig. 11. Breaking process curves of fibers (m=4) with varying initial L/D ratios (D=1 mm and L varying). (a) Number of fractures with increasing tensile strain of the composite; (b) Number of fractures at fracture saturation as a function of initial L/D ratio; (c) Mean fracture spacing at fracture saturation as a function of initial L/D ratio; and (d) Relationship between the mean S/D ratio at fracture saturation and the volume fraction of fiber.

Fig. 12. The breaking process for the fiber with L=8 mm and D=1 mm (length of each microboudin in mm). See the text for detailed explanation.

Fig. 13. Breaking processes for fibers with constant diameter but different lengths. The number of fractures is indicated as the tensile strain increases.

Fig. 14. Fracture distribution in fibers with constant length but different L/D ratios at saturation. The model dimensions are 6×6×12 mm^3, with a model unit of 120×120×240. The fiber and matrix heterogeneity indices are m=4 and 6, respectively. Tensile stresses are shown in red and orange-red, while compressive stresses are shown in yellow, green, and blue. The number indicated in each sub-figure represents the occurrence sequence of fractures.

Fig. 15. Breaking process curves for fibers with a constant length (L=8 mm) but varying diameters (L/D=2, 4, 6, 8, 10, 15, and 20). In (a), the variation in the number of fractures among fibers with different L/D ratios is shown as the tensile strain increases. (b) presents the relationship between the number of fractures at fracture saturation and the L/W ratio. (c) displays the average fracture spacing at fracture saturation as a function of the L/D ratio. (d) illustrates the relationship between the fracture spacing-to-diameter ratio (S/D) and the L/D ratio.

Fig. 16. Cloud diagrams of the maximum principal stress and fracture distribution in fibers with different heterogeneity indices at saturation. The model dimensions are 4×4×12 mm^3, with a model unit of 80×80×240. Tensile stresses are shown in red and orange-red, while compressive stresses are shown in yellow, green, and blue. The number indicated in each sub-figure represents the occurrence sequence of fractures.

Figure S1. The Weibull distributions with varying shape coefficients (m=1.2, 3.0, 6.0, and ∞). In this diagram, f(u) represents the probability density function of the material parameter u, such as strength or elastic modulus, while u_0 denotes the mean value of u. As the m value increases, also known as the material homogeneity index, the range of the u distribution becomes narrower around the average value (u_0). This narrowing indicates a higher level of material uniformity.

Figure S2. Effects of material homogeneity index (m) on the distributions of Young's Modulus for a model with a mean value of 56 GPa. (a) m=1.2; (b) m=6.0. Please refer to the text for further explanation.

Figure S3. A schematic illustration of the constitutive law governing a mesoscopic element of a brittle fiber subjected to uniaxial compressive and tensile stresses. The symbols σ_{c0} and σ_{t0} represent the compressive and tensile strengths, respectively. Similarly, σ_{cr} and σ_{tr} denote the residual compressive strength and residual tensile strength. ε_{tu} represents the ultimate tensile strain, while ε_{c0} and ε_{t0} represent the strains at the elastic limit under compression and tension, respectively.

Figure S4. A cloud diagram illustrating the minimum principal stress for various models with different ratios of fracture spacing to fiber diameter (S/D). The sections depicted in the diagram are cut parallel to the X- and Z-axes. The model dimensions are 4×4×12 mm^3, and the unit of the model is 120×120×360, resulting in a total of 5,184,000 units. The color-scale in the diagram represents different stress magnitudes.

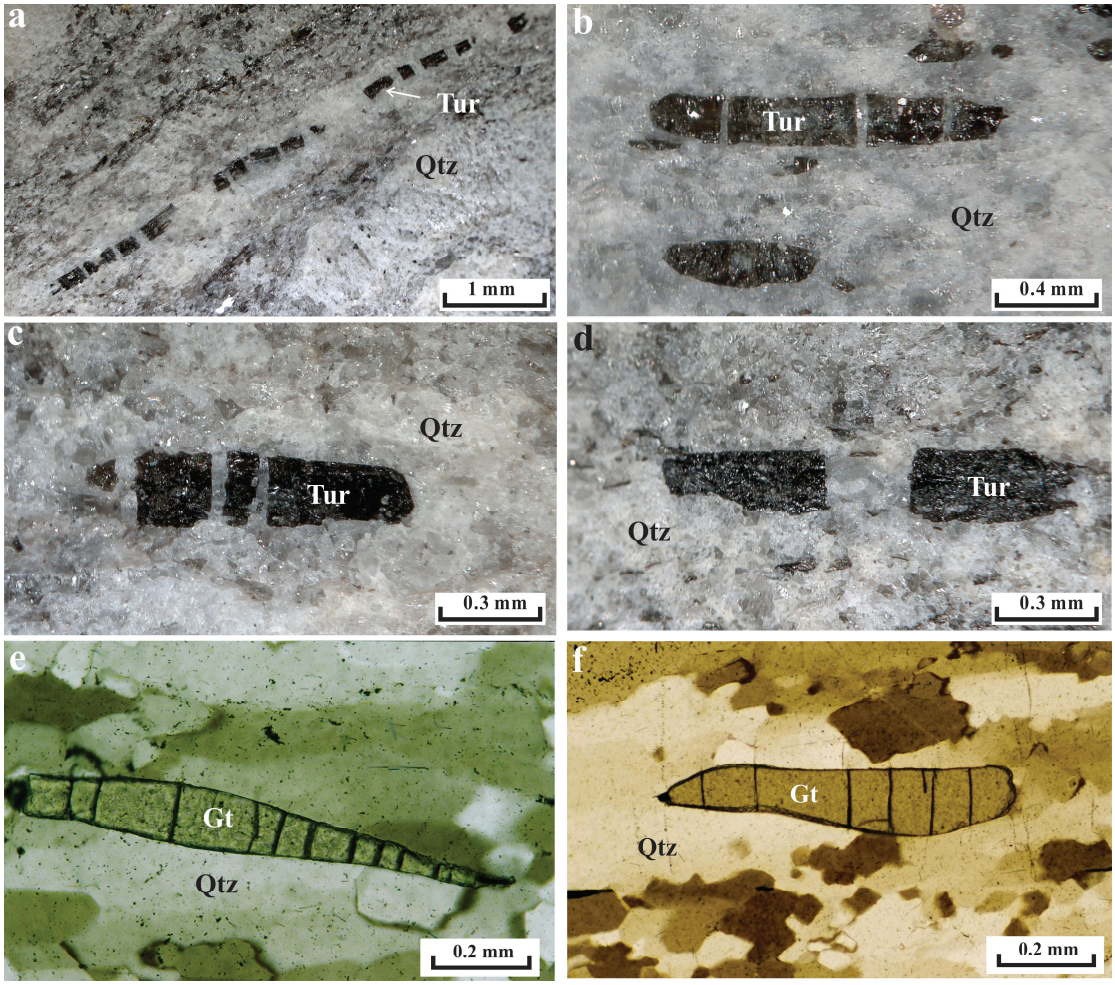
a
Tur
Qtz
1 mm
b
Tur
Qtz
0.4 mm
c
Qtz
Tur
0.3 mm
d
Tur
Qtz
0.3 mm
e
Gt
Qtz
0.2 mm
f
Gt
Qtz
0.2 mm

Fig.1

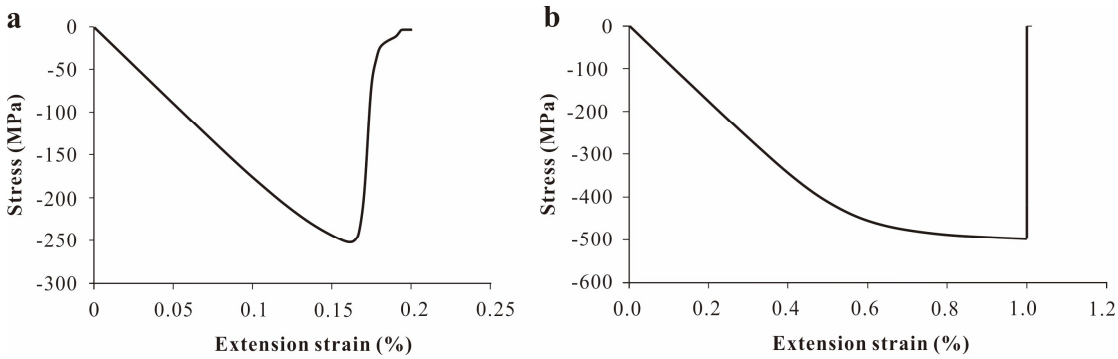
a
Stress (MPa)
0
-50
-100
-150
-200
-250
-300
0
0.05
0.1
0.15
0.2
0.25
Extension strain (%)
b
Stress (MPa)
0
-100
-200
-300
-400
-500
-600
0.0
0.2
0.4
0.6
0.8
1.0
1.2
Extension strain (%)

Fig.2

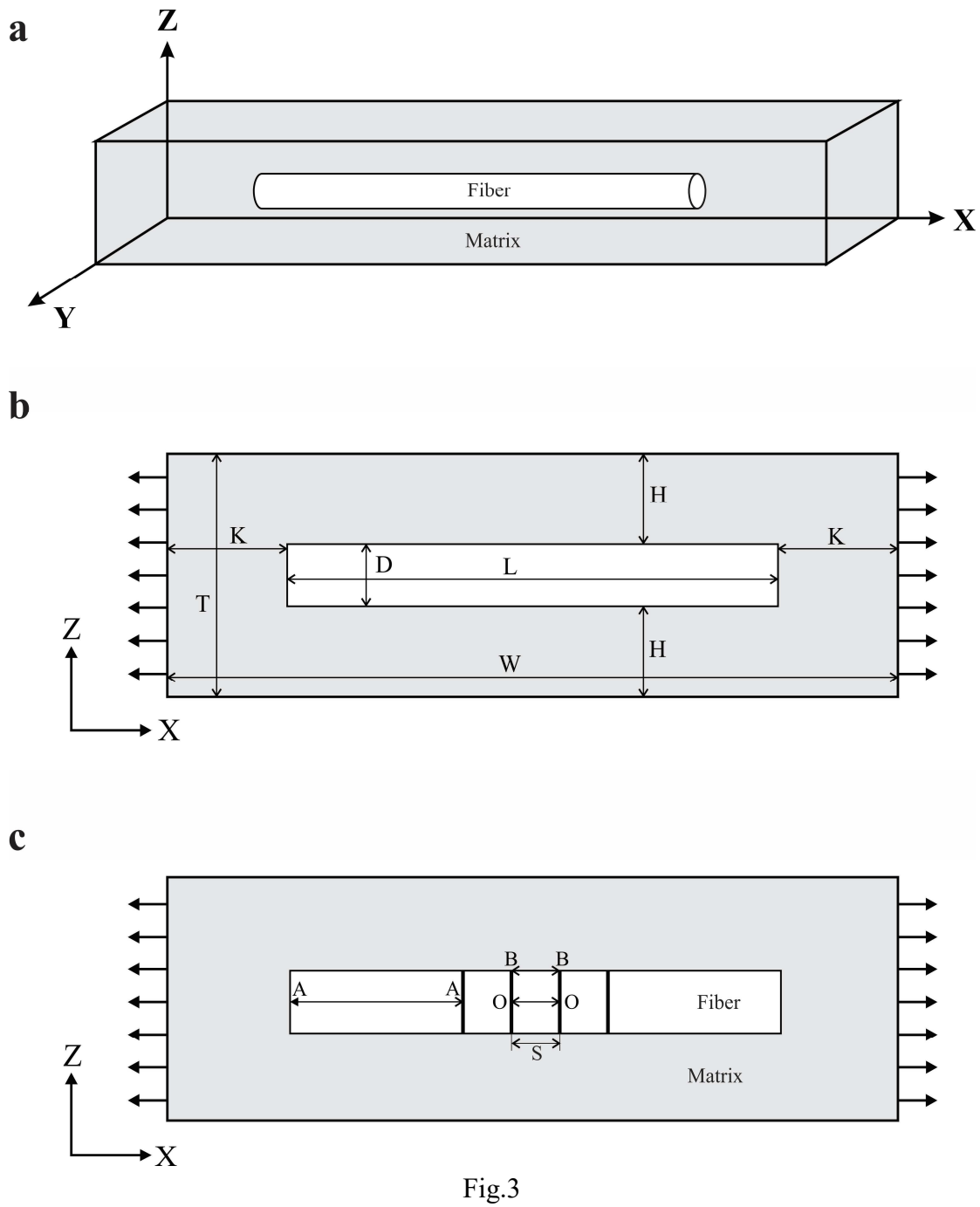

Fig.3

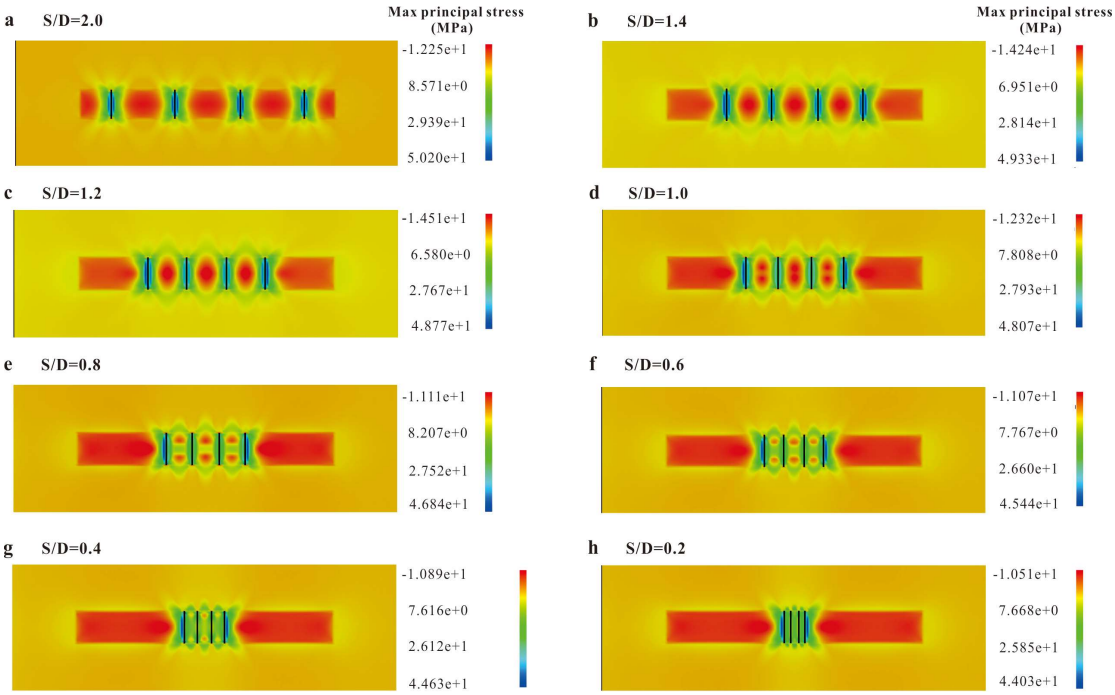
a S/D=2.0
Max principal stress (MPa)
-1.225e+1
8.571e+0
2.939e+1
5.020e+1
b S/D=1.4
Max principal stress (MPa)
-1.424e+1
6.951e+0
2.814e+1
4.933e+1
c S/D=1.2
-1.451e+1
6.580e+0
2.767e+1
4.877e+1
d S/D=1.0
-1.232e+1
7.808e+0
2.793e+1
4.807e+1
e S/D=0.8
-1.111e+1
8.207e+0
2.752e+1
4.684e+1
f S/D=0.6
-1.107e+1
7.767e+0
2.660e+1
4.544e+1
g S/D=0.4
-1.089e+1
7.616e+0
2.612e+1
4.463e+1
h S/D=0.2
-1.051e+1
7.668e+0
2.585e+1
4.403e+1

Fig.4

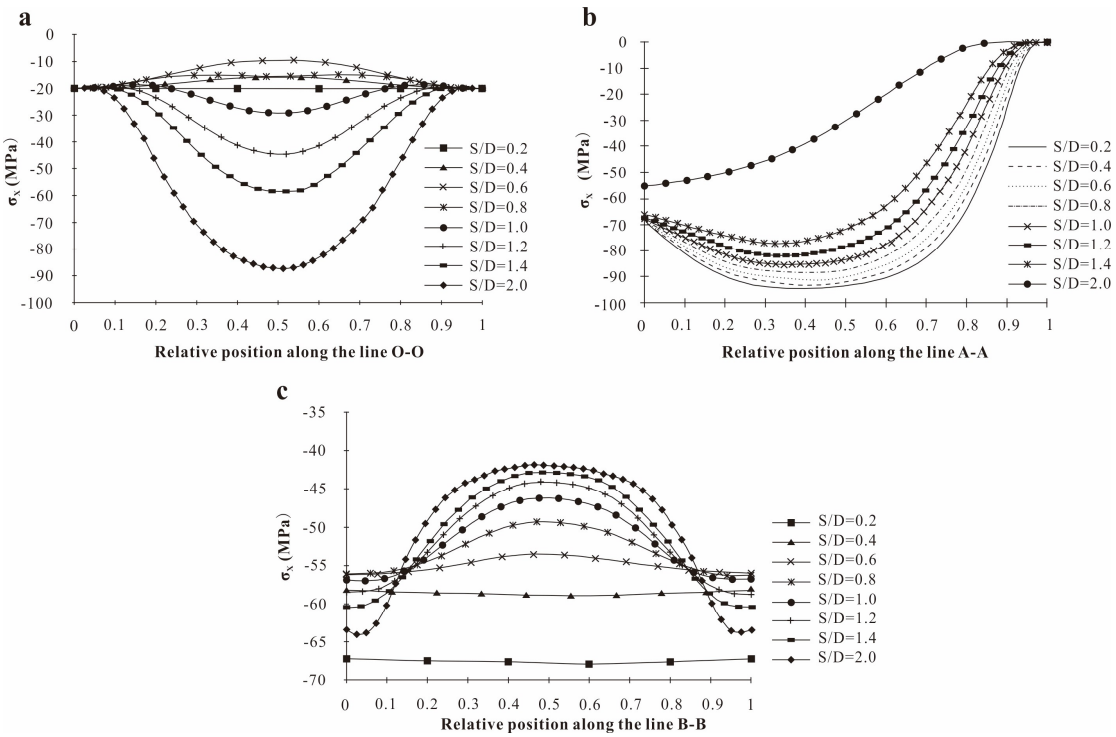
a
0
-10
-20
-30
-40
-50
-60
-70
-80
-90
-100
σx (MPa)
0 0.1 0.2 0.3 0.4 0.5 0.6 0.7 0.8 0.9 1
Relative position along the line O-O
S/D=0.2
S/D=0.4
S/D=0.6
S/D=0.8
S/D=1.0
S/D=1.2
S/D=1.4
S/D=2.0
b
0
-10
-20
-30
-40
-50
-60
-70
-80
-90
-100
σx (MPa)
0 0.1 0.2 0.3 0.4 0.5 0.6 0.7 0.8 0.9 1
Relative position along the line A-A
S/D=0.2
S/D=0.4
S/D=0.6
S/D=0.8
S/D=1.0
S/D=1.2
S/D=1.4
S/D=2.0
c
-35
-40
-45
-50
-55
-60
-65
-70
σx (MPa)
0 0.1 0.2 0.3 0.4 0.5 0.6 0.7 0.8 0.9 1
Relative position along the line B-B
S/D=0.2
S/D=0.4
S/D=0.6
S/D=0.8
S/D=1.0
S/D=1.2
S/D=1.4
S/D=2.0

Fig.5

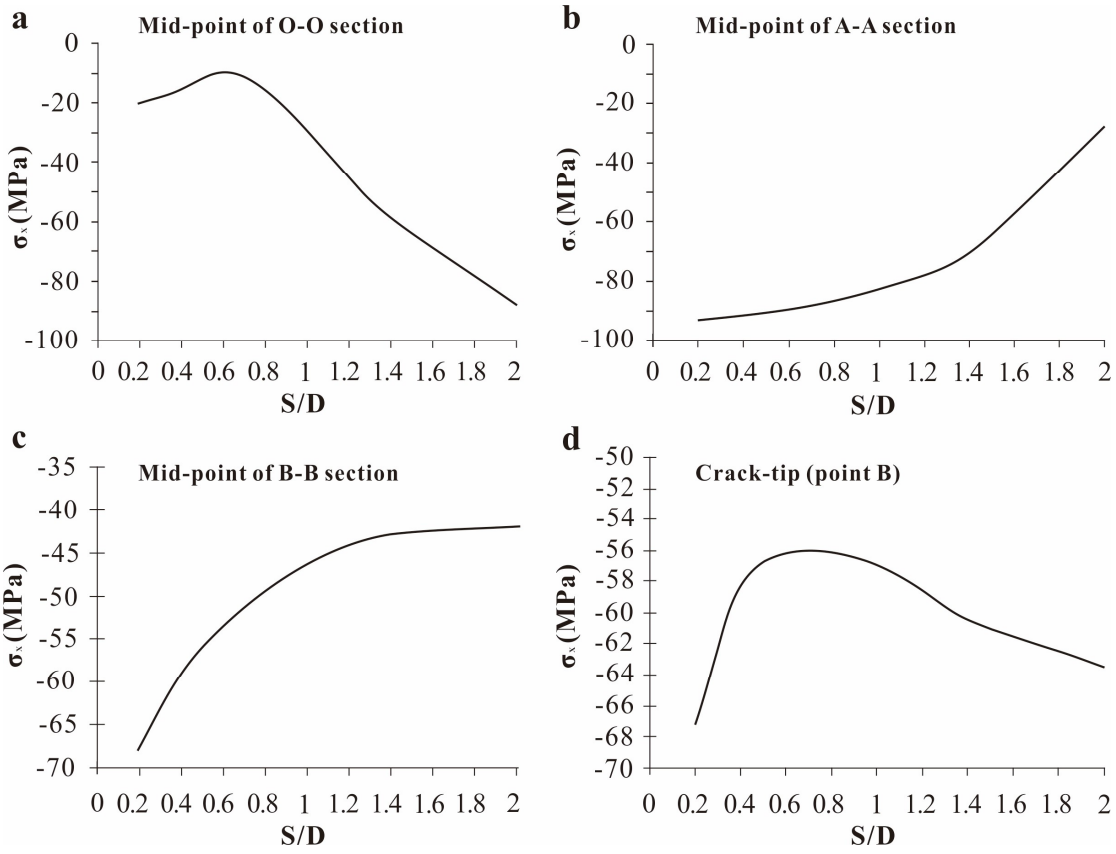
a
Mid-point of O-O section
σx(MPa)
0
-20
-40
-60
-80
-100
0 0.2 0.4 0.6 0.8 1 1.2 1.4 1.6 1.8 2
S/D
b
Mid-point of A-A section
σx(MPa)
0
-20
-40
-60
-80
-100
0 0.2 0.4 0.6 0.8 1 1.2 1.4 1.6 1.8 2
S/D
c
Mid-point of B-B section
σx(MPa)
-35
-40
-45
-50
-55
-60
-65
-70
0 0.2 0.4 0.6 0.8 1 1.2 1.4 1.6 1.8 2
S/D
d
Crack-tip (point B)
σx(MPa)
-50
-52
-54
-56
-58
-60
-62
-64
-66
-68
-70
0 0.2 0.4 0.6 0.8 1 1.2 1.4 1.6 1.8 2
S/D

Fig.6

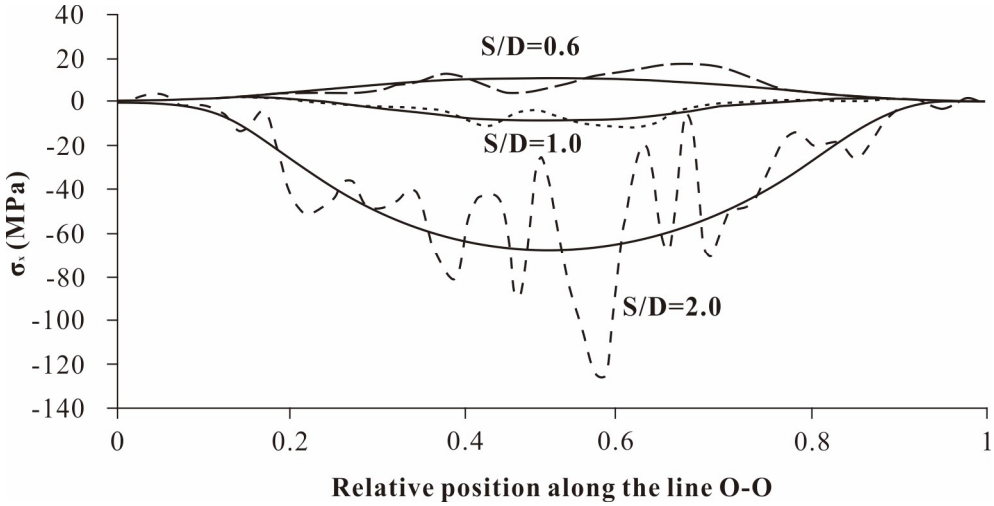
40
20
0
-20
-40
-60
-80
-100
-120
-140
σ. (MPa)
S/D=0.6
S/D=1.0
S/D=2.0
0
0.2
0.4
0.6
0.8
1
Relative position along the line O-O
Fig.7

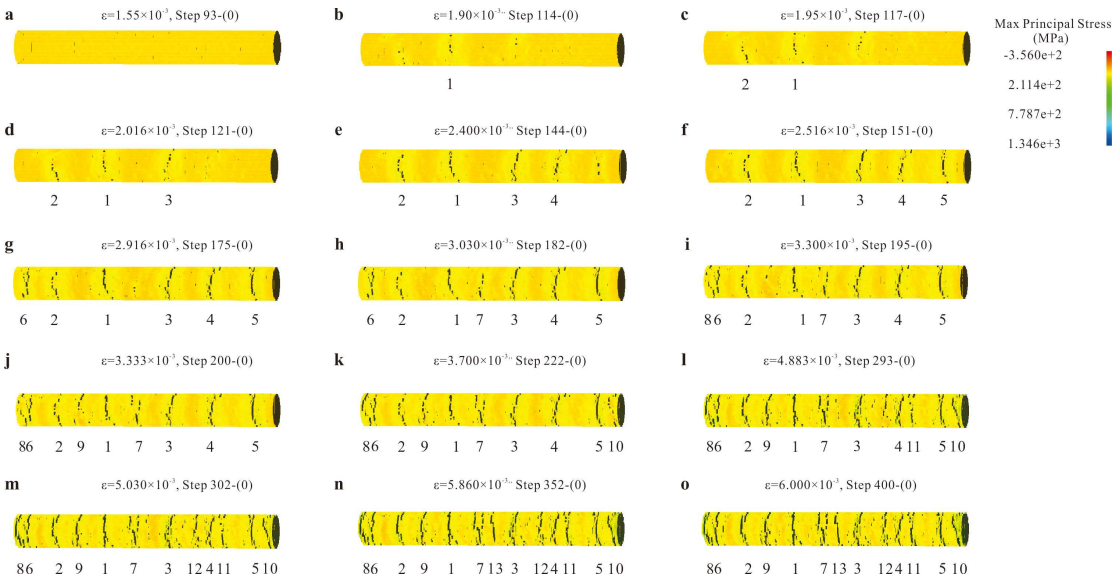
a
ε=1.55×10⁻³, Step 93-(0)
b
ε=1.90×10⁻³, Step 114-(0)
1
c
ε=1.95×10⁻³, Step 117-(0)
2 1
Max Principal Stress (MPa)
-3.560e+2
2.114e+2
7.787e+2
1.346e+3
d
ε=2.016×10⁻³, Step 121-(0)
2 1 3
e
ε=2.400×10⁻³, Step 144-(0)
2 1 3 4
f
ε=2.516×10⁻³, Step 151-(0)
2 1 3 4 5
g
ε=2.916×10⁻³, Step 175-(0)
6 2 1 3 4 5
h
ε=3.030×10⁻³, Step 182-(0)
6 2 1 7 3 4 5
i
ε=3.300×10⁻³, Step 195-(0)
86 2 1 7 3 4 5
j
ε=3.333×10⁻³, Step 200-(0)
86 2 9 1 7 3 4 5
k
ε=3.700×10⁻³, Step 222-(0)
86 2 9 1 7 3 4 5 10
l
ε=4.883×10⁻³, Step 293-(0)
86 2 9 1 7 3 4 11 5 10
m
ε=5.030×10⁻³, Step 302-(0)
86 2 9 1 7 3 12 4 11 5 10
n
ε=5.860×10⁻³, Step 352-(0)
86 2 9 1 7 13 3 12 4 11 5 10
o
ε=6.000×10⁻³, Step 400-(0)
86 2 9 1 7 13 3 12 4 11 5 10

Fig.8

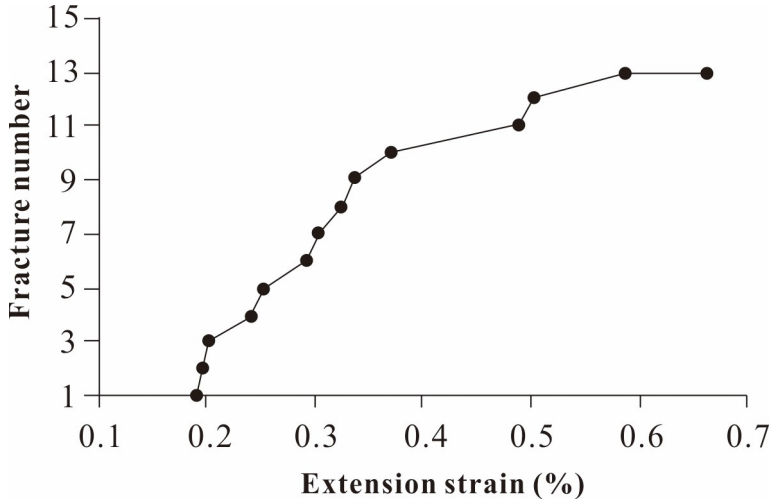
15
13
11
9
7
5
3
1
Fracture number
0.1
0.2
0.3
0.4
0.5
0.6
0.7
Extension strain (%)
Fig.9

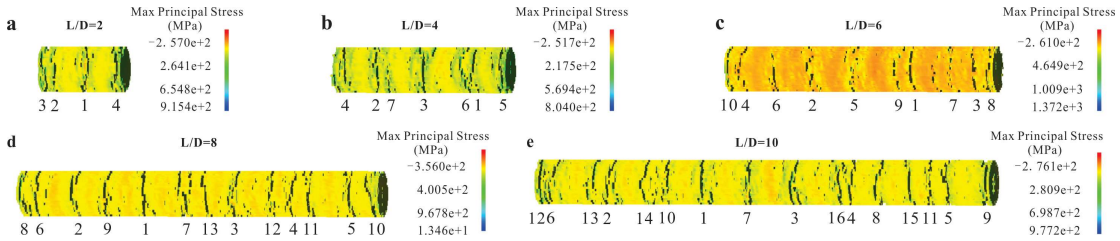
a
L/D=2
Max Principal Stress
(MPa)
−2. 570e+2
2.641e+2
6.548e+2
9.154e+2
3 2 1 4
b
L/D=4
Max Principal Stress
(MPa)
−2. 517e+2
2.175e+2
5.694e+2
8.040e+2
4 2 7 3 6 1 5
c
L/D=6
Max Principal Stress
(MPa)
−2. 610e+2
4.649e+2
1.009e+3
1.372e+3
10 4 6 2 5 9 1 7 3 8
d
L/D=8
Max Principal Stress
(MPa)
−3.560e+2
4.005e+2
9.678e+2
1.346e+1
8 6 2 9 1 7 13 3 12 4 11 5 10
e
L/D=10
Max Principal Stress
(MPa)
−2. 761e+2
2.809e+2
6.987e+2
9.772e+2
126 13 2 14 10 1 7 3 164 8 15 11 5 9

Fig.10

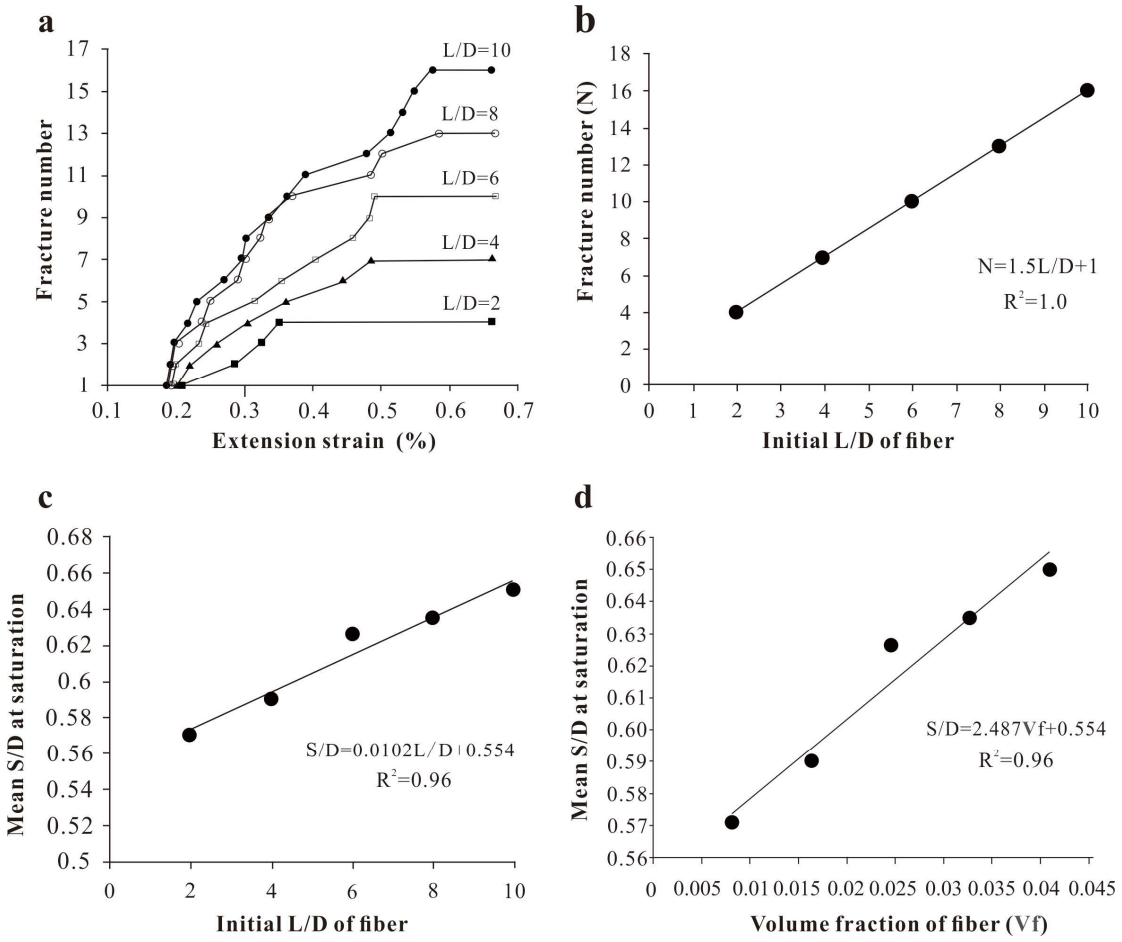
a
Fracture number
Extension strain (%)
L/D=10
L/D=8
L/D=6
L/D=4
L/D=2
b
Fracture number (N)
Initial L/D of fiber
N=1.5L/D+1
R²=1.0
c
Mean S/D at saturation
Initial L/D of fiber
S/D=0.0102L/D+0.554
R²=0.96
d
Mean S/D at saturation
Volume fraction of fiber (Vf)
S/D=2.487Vf+0.554
R²=0.96

Fig.11

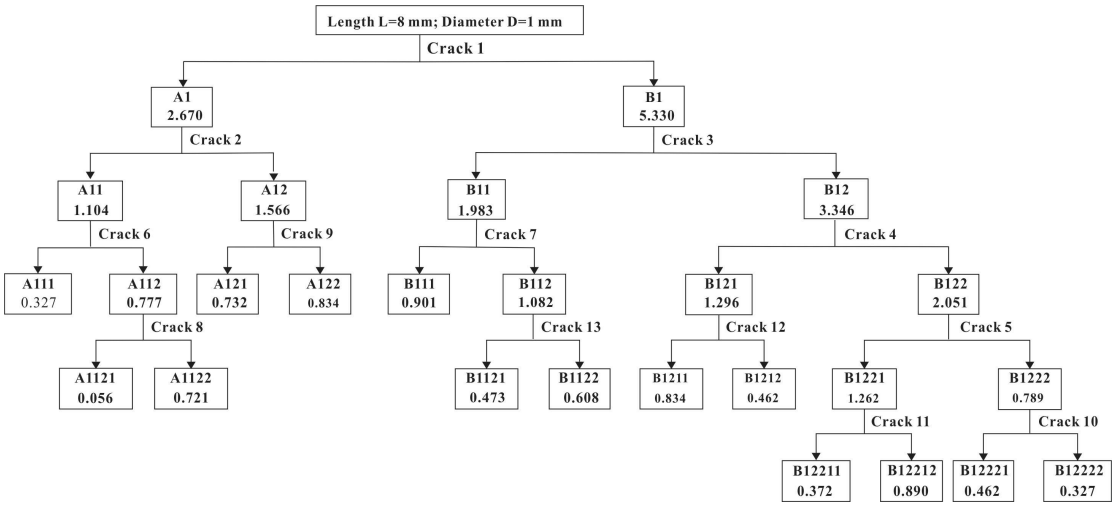
Length L=8 mm; Diameter D=1 mm
Crack 1
A1
2.670
B1
5.330
Crack 2
Crack 3
A11
1.104
A12
1.566
B11
1.983
B12
3.346
Crack 6
Crack 9
Crack 7
Crack 4
A111
0.327
A112
0.777
A121
0.732
A122
0.834
B111
0.901
B112
1.082
B121
1.296
B122
2.051
Crack 8
Crack 13
Crack 12
Crack 5
A1121
0.056
A1122
0.721
B1121
0.473
B1122
0.608
B1211
0.834
B1212
0.462
B1221
1.262
B1222
0.789
Crack 11
Crack 10
B12211
0.372
B12212
0.890
B12221
0.462
B12222
0.327

Fig.12

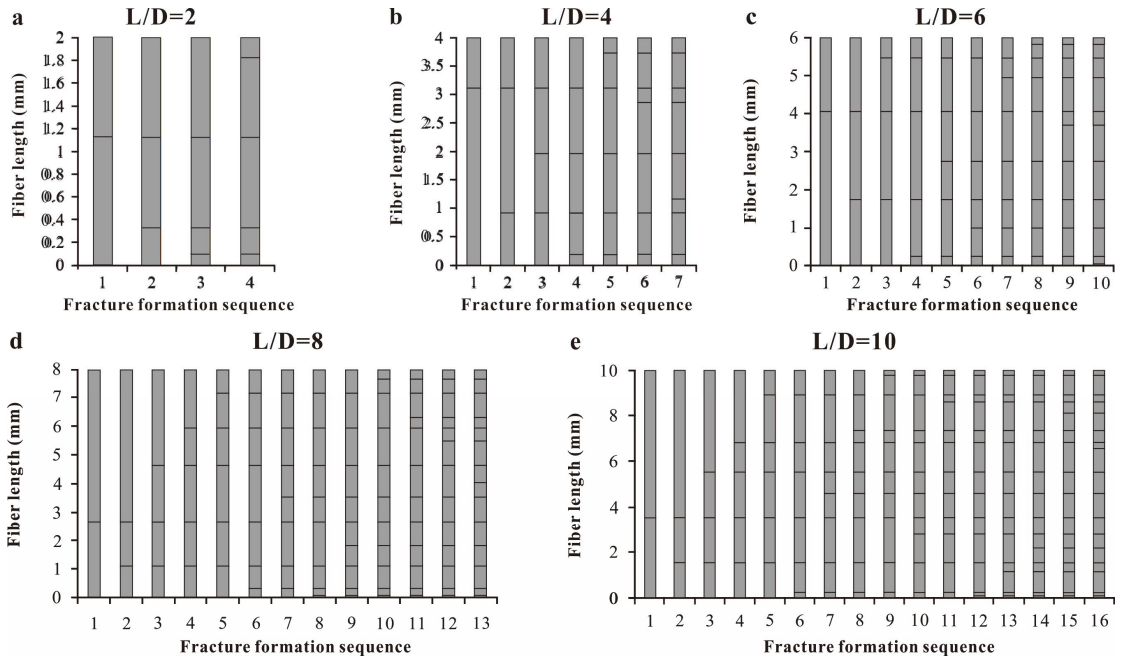
a
L/D=2
Fiber length (mm)
Fracture formation sequence
b
L/D=4
Fiber length (mm)
Fracture formation sequence
c
L/D=6
Fiber length (mm)
Fracture formation sequence
d
L/D=8
Fiber length (mm)
Fracture formation sequence
e
L/D=10
Fiber length (mm)
Fracture formation sequence

Fig.13

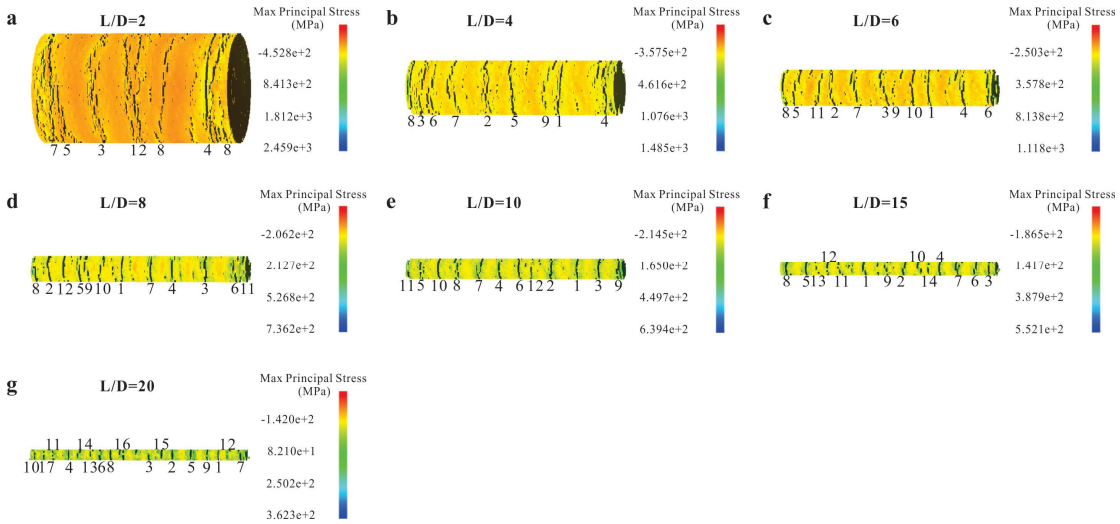
a
L/D=2
Max Principal Stress (MPa)
-4.528e+2
8.413e+2
1.812e+3
2.459e+3
7 5 3 12 8 4 8
b
L/D=4
Max Principal Stress (MPa)
-3.575e+2
4.616e+2
1.076e+3
1.485e+3
8 3 6 7 2 5 9 1 4
c
L/D=6
Max Principal Stress (MPa)
-2.503e+2
3.578e+2
8.138e+2
1.118e+3
8 5 11 2 7 3 9 10 1 4 6
d
L/D=8
Max Principal Stress (MPa)
-2.062e+2
2.127e+2
5.268e+2
7.362e+2
8 2 12 5 9 10 1 7 4 3 6 11
e
L/D=10
Max Principal Stress (MPa)
-2.145e+2
1.650e+2
4.497e+2
6.394e+2
11 5 10 8 7 4 6 12 2 1 3 9
f
L/D=15
Max Principal Stress (MPa)
-1.865e+2
1.417e+2
3.879e+2
5.521e+2
12 10 4
8 5 13 11 1 9 2 14 7 6 3
g
L/D=20
Max Principal Stress (MPa)
-1.420e+2
8.210e+1
2.502e+2
3.623e+2
11 14 16 15 12
10 17 4 13 6 8 3 2 5 9 1 7

Fig.14

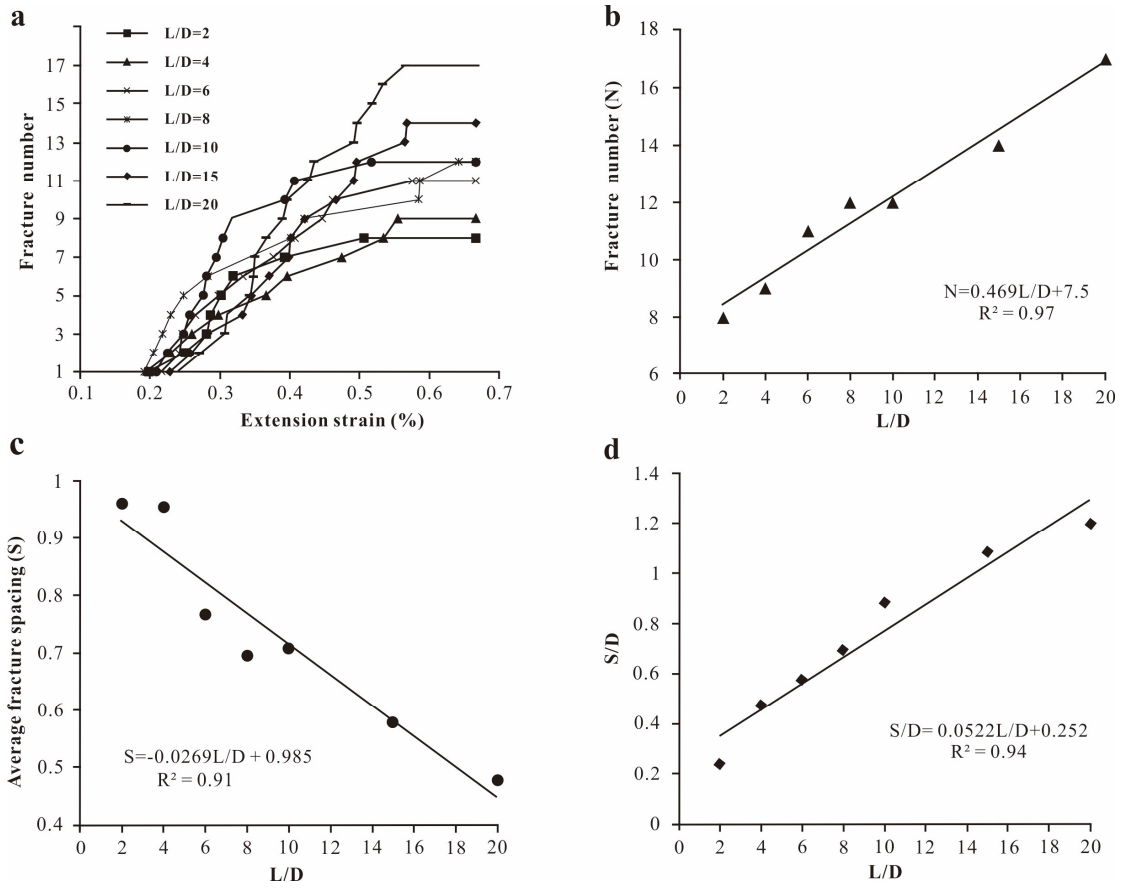
a
L/D=2
L/D=4
L/D=6
L/D=8
L/D=10
L/D=15
L/D=20
Fracture number
Extension strain (%)
b
Fracture number (N)
N=0.469L/D+7.5
R² = 0.97
L/D
c
Average fracture spacing (S)
S=-0.0269L/D + 0.985
R² = 0.91
L/D
d
S/D
S/D= 0.0522L/D+0.252
R² = 0.94
L/D

Fig.15

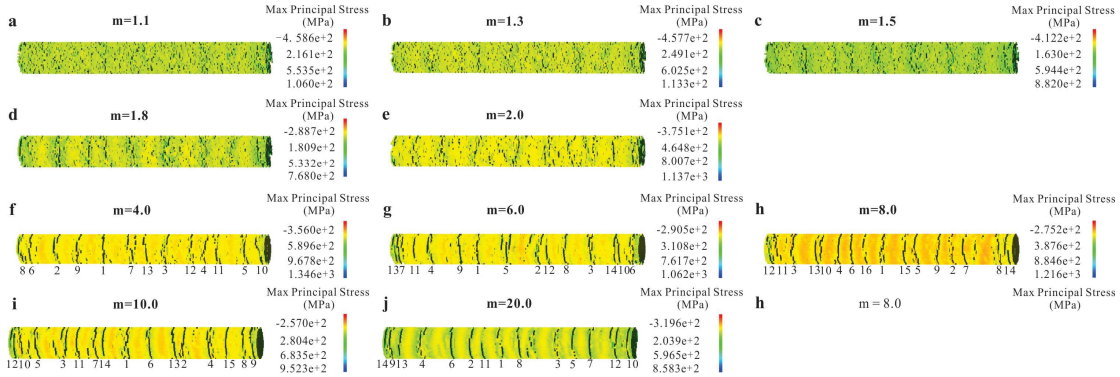
a
m=1.1
Max Principal Stress (MPa)
−4. 586e+2
2.161e+2
5.535e+2
1.060e+2
b
m=1.3
Max Principal Stress (MPa)
-4.577e+2
2.491e+2
6.025e+2
1.133e+2
c
m=1.5
Max Principal Stress (MPa)
-4.122e+2
1.630e+2
5.944e+2
8.820e+2
d
m=1.8
Max Principal Stress (MPa)
-2.887e+2
1.809e+2
5.332e+2
7.680e+2
e
m=2.0
Max Principal Stress (MPa)
-3.751e+2
4.648e+2
8.007e+2
1.137e+3
f
m=4.0
Max Principal Stress (MPa)
-3.560e+2
5.896e+2
9.678e+2
1.346e+3
8 6 2 9 1 7 13 3 12 4 11 5 10
g
m=6.0
Max Principal Stress (MPa)
-2.905e+2
3.108e+2
7.617e+2
1.062e+3
137 11 4 9 1 5 212 8 3 14106
h
m=8.0
Max Principal Stress (MPa)
-2.752e+2
3.876e+2
8.846e+2
1.216e+3
1211 3 13 0 4 6 16 1 15 5 9 2 7 8 14
i
m=10.0
Max Principal Stress (MPa)
-2.570e+2
2.804e+2
6.835e+2
9.523e+2
1210 5 3 11 714 1 6 132 4 15 8 9
j
m=20.0
Max Principal Stress (MPa)
-3.196e+2
2.039e+2
5.965e+2
8.583e+2
14913 4 6 2 11 1 8 3 5 7 12 10
h
m = 8.0
Max Principal Stress (MPa)

Fig.16

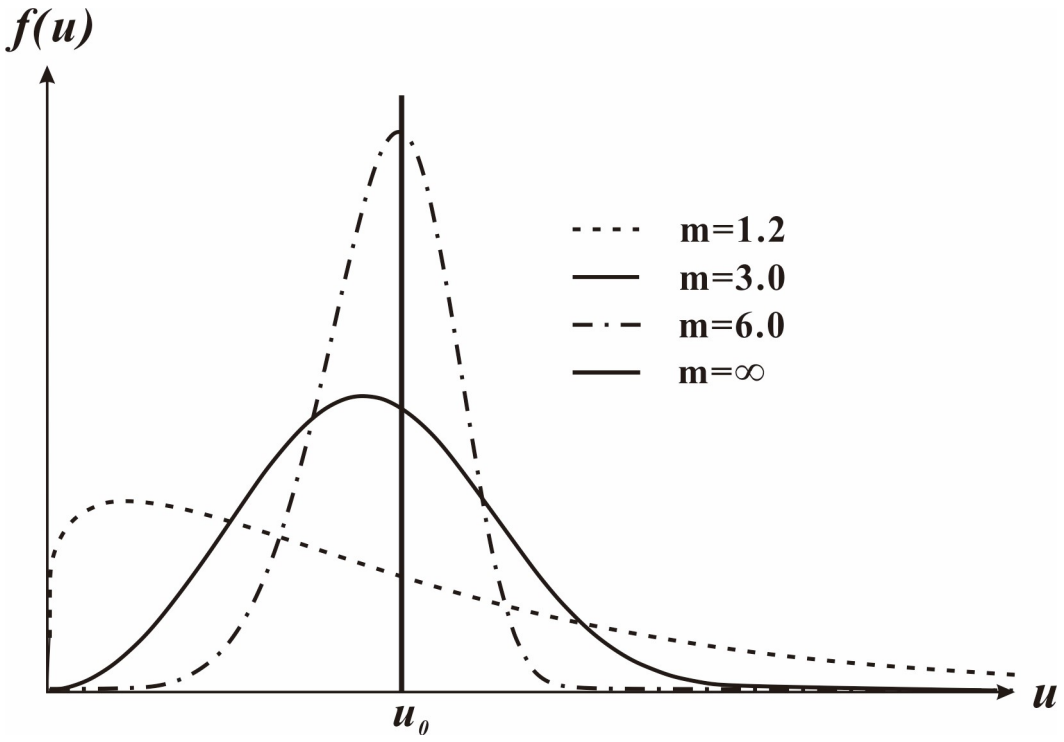

Fig.S1

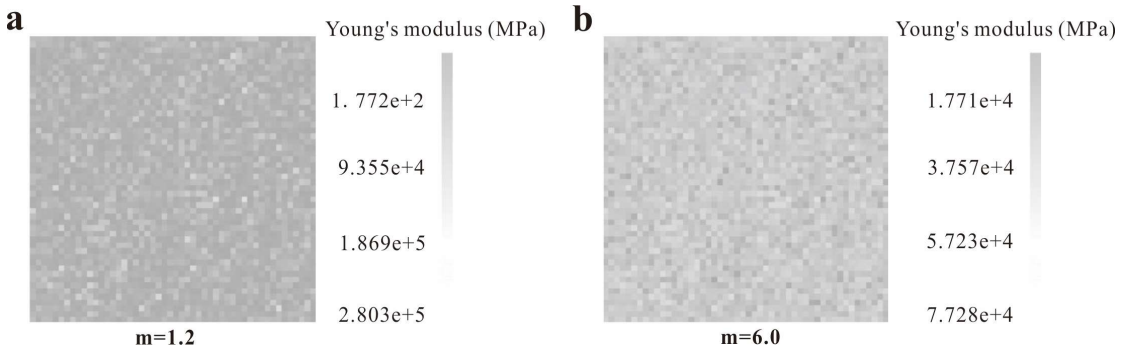
a
Young's modulus (MPa)
1. 772e+2
9.355e+4
1.869e+5
2.803e+5
m=1.2
b
Young's modulus (MPa)
1.771e+4
3.757e+4
5.723e+4
7.728e+4
m=6.0

Fig.S2

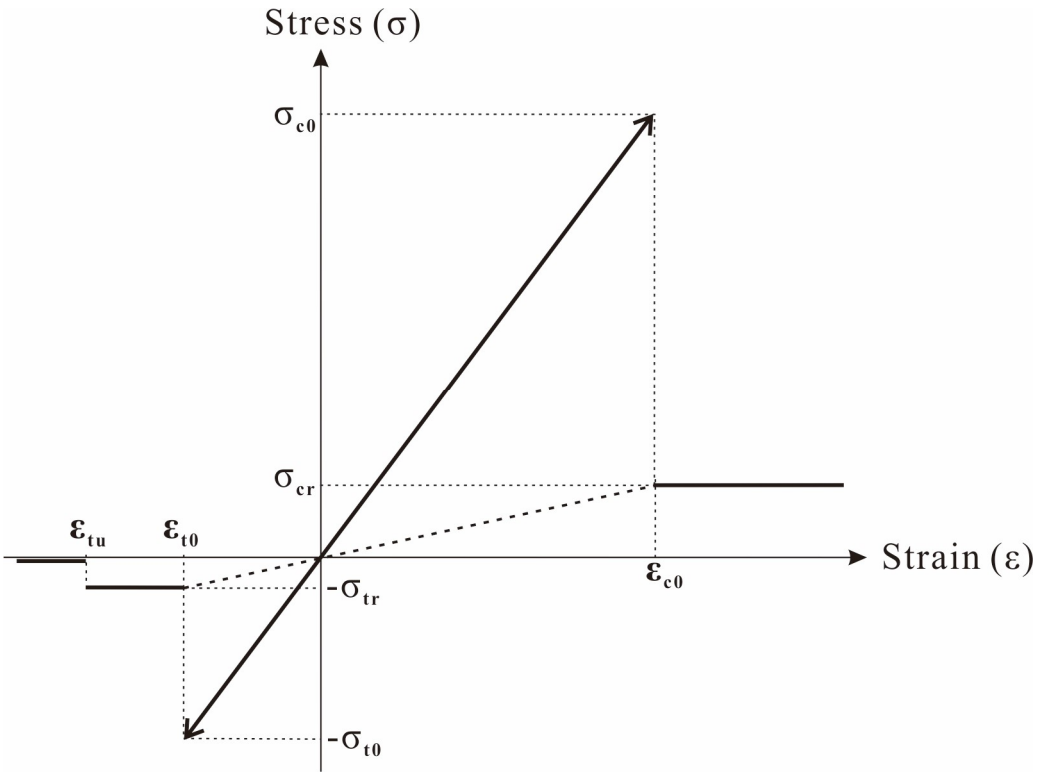

Fig.S3

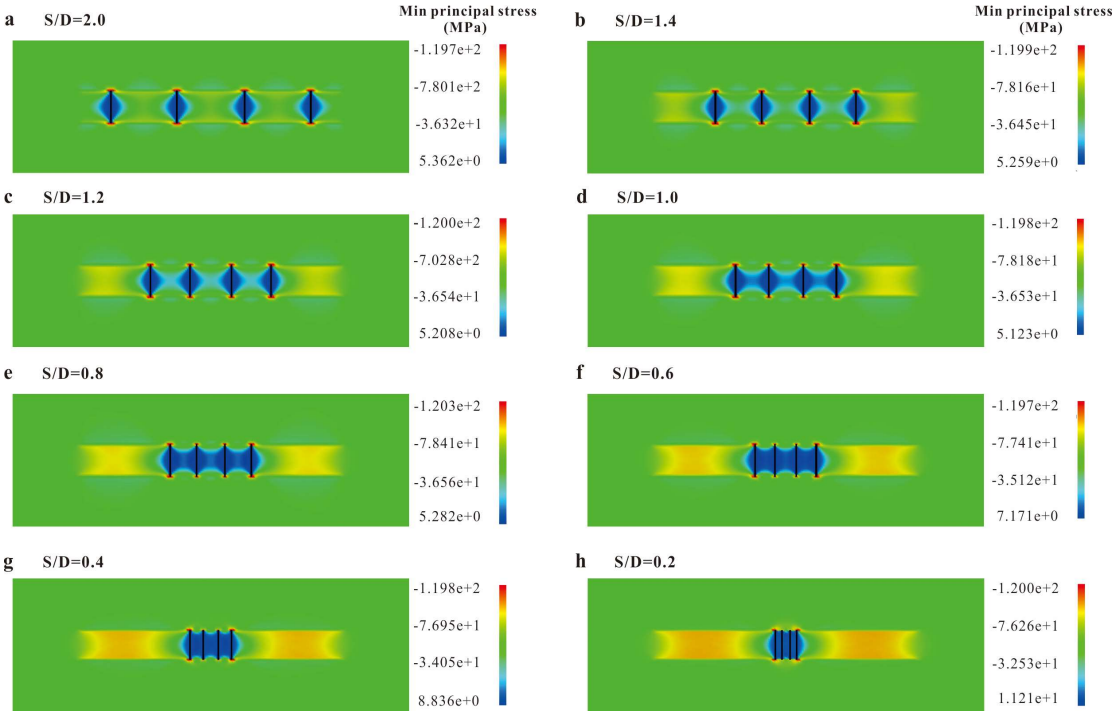
a S/D=2.0
Min principal stress (MPa)
-1.197e+2
-7.801e+2
-3.632e+1
5.362e+0
b S/D=1.4
Min principal stress (MPa)
-1.199e+2
-7.816e+1
-3.645e+1
5.259e+0
c S/D=1.2
-1.200e+2
-7.028e+2
-3.654e+1
5.208e+0
d S/D=1.0
-1.198e+2
-7.818e+1
-3.653e+1
5.123e+0
e S/D=0.8
-1.203e+2
-7.841e+1
-3.656e+1
5.282e+0
f S/D=0.6
-1.197e+2
-7.741e+1
-3.512e+1
7.171e+0
g S/D=0.4
-1.198e+2
-7.695e+1
-3.405e+1
8.836e+0
h S/D=0.2
-1.200e+2
-7.626e+1
-3.253e+1
1.121e+1

Fig.S4

Table 1. Geometry and mechanical parameters of tourmaline and quartz (gem-quality single crystals).

Material	E (GPa)	Poisson's ratio	σ_t (MPa)	σ_c (GPa)	λ	Size (mm^3)
Fiber (tourmaline)	201.5	0.24	580	5.8	0.1	$\pi \times 0.5^2 \times 8$
Matrix (quartz)	95.6	0.08	555	5.55	1	$4 \times 4 \times 12$